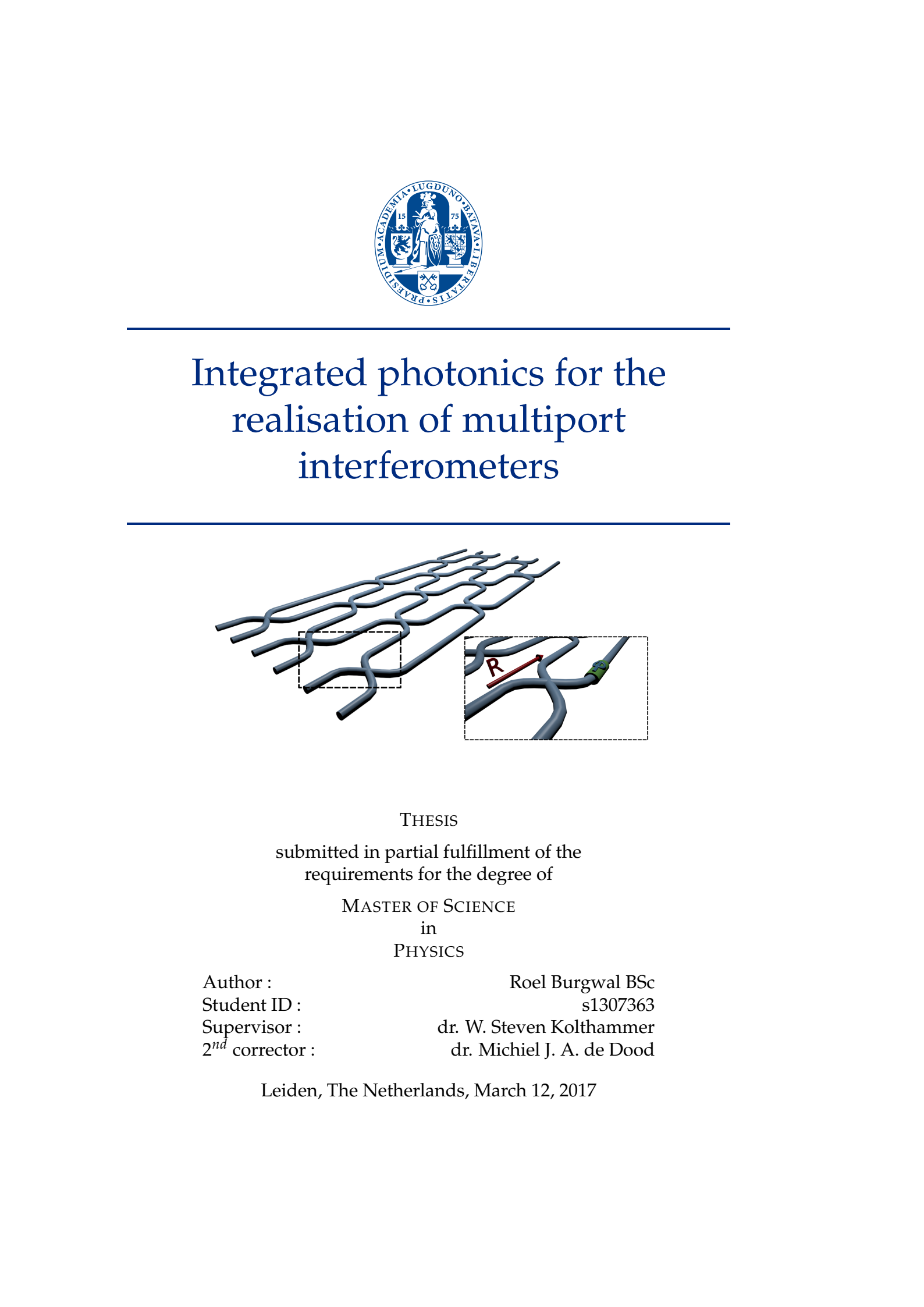

Integrated photonics for the realisation of multiport interferometers

THESIS

submitted in partial fulfillment of the
requirements for the degree of

MASTER OF SCIENCE
in
PHYSICS

Author :	Roel Burgwal BSc
Student ID :	s1307363
Supervisor :	dr. W. Steven Kolthammer
2^{nd} corrector :	dr. Michiel J. A. de Dood

Leiden, The Netherlands, March 12, 2017

Integrated photonics for the realisation of multiport interferometers

Roel Burgwal BSc

Huygens-Kamerlingh Onnes Laboratory, Leiden University
P.O. Box 9500, 2300 RA Leiden, The Netherlands

March 12, 2017

Abstract

Multiport interferometers are an inportant tool in the emerging field of quantum information technologies. In theoretical work, we investigate implementing Haar-random unitary transformations in increasingly large interferometers with realistic imperfections. We find that random matrices result in mostly low values of interferometer beam splitter reflectivities. We model production imperfections and we find that these severely limit the implementation of random matrices. We show the effects of the imperfection can be mitigated through optimisation of interferometer degrees of freedom and by adding additional beam splitters. In experimental work, we investigate the realisation of reconfigurable multiport interferometers in silica-on-silicon integrated photonics chips using a modular design. We show that individual modules are fully reconfigurable. We give a proof-of-principle of the design by connecting three modules for the first time and measure $\approx 5\%$ transmission.

Contents

Version of March 12, 2017– Created March 12, 2017 - 20:35

Version of March 12, 2017– Created March 12, 2017 - 20:35

Chapter 1

Introduction

This report describes research conducted in the Ultrafast Quantum Optics (UQO) group at the University of Oxford between August and December 2016. The UQO group is led by prof I.A. Walmsley. The local supervisor was dr W.S. Kolthammer. Day-to-day supervision was provided by dr J.J. Renema and W.R.Clements, who also deserve credit for the findings presented here.

Quantum technologies will be one of the major advances of science in the 21st century. In the previous century, we discovered quantum physics and found the laws that describe a quantum system. In the eighties, it was suggested that we might use this knowledge to perform calculations using quantum systems [1–3]. This idea sparked interest, leading to the development of algorithms that could be performed using a quantum system, now called a quantum computer. Two famous examples are Shor's algorithm for factoring numbers [4] and Grover's algorithm for searching databases [5]. The most interesting property of these quantum algorithms is that they are expected to solve the problem in question faster than a classical (i.e. non-quantum) algorithm. More precisely, while the classical computation time for prime factorisation is strongly believed to be exponential in the input size, the quantum computation will scale polynomial with the input size. Thus, these algorithms show that a quantum computer could outrun any classical computer if the input size is large enough.

One of the fields of research is photonic quantum technologies, in which the quantum states of photons are used to perform computations or to communicate. Compared to other implementations, such as trapped ions [6] and superconducting currents [7], photons have two advantages: they suffer very little environmental decoherence and are the best way

to send quantum states over long distance. Manipulation of photonic quantum states will therefore always be needed to realise quantum communication.

This work revolves around multiport interferometers. These devices with multiple input ports (multiport), produced using integrated photonics, are one of the photonic quantum technologies currently under development. The interferometers can be used to perform operations on quantum states of light, which has numerous applications in quantum information science. They have been used to implement qubit operations [9], with which one can perform a.o. quantum teleportation [8] or quantum key distribution [10].

Here, we report experimental and theoretical work done on multiport interferometers. Experimental work consists of characterising reconfigurable interferometers produced by the University of Southampton. These interferometers are designed to be constructed from building blocks called modules. We determine losses inside these modules and losses from coupling light from fiber into the modules. We also test the reconfigurability of the individual modules and show that a reconfigurability range can be achieved that is large enough for all purposes.

Next, we connect three modules to produce several 3-mode reconfigurable interferometers. This is the first time the assembly of a modular interferometer design was performed. The transmission through the assembly is determined. We conclude that the modular design concept works. Several challenges remain, however, the largest of which is decreasing the losses in the interferometer.

This report is structured as follows. First, chapter 2 introduces multiport interferometers and the theoretical concepts needed to understand this work. Next, chapter 3 is a self-contained report of theoretical work on random transformations in multiport interferometers. Chapter 4 introduces the platform on which the interferometer is constructed: silica-on-silicon integrated photonics chips. After that, chapter 5 reports on measurements performed on the photonics chips produced by the University of Southampton.

Chapter 2

Optical interferometers

2.1 Reconfigurable multiport interferometers

A multiport interferometer interferes a number of spatially separated input ports, which we call modes. The state of the system in the input modes is changed to a different state at the output modes. An example can be seen in figure 2.1. A light is sent into the input modes from the left.

Through beam splitters (see blue close-up in figure), the different modes couple to each other and are allowed to interfere. At the other end of the interferometer, the output light is detected. The idea of a reconfigurable interferometer is that the reflectivities of the beam splitters are adjustable. By tuning these values, the effect of the interferometer is altered.

Additionally, the interferometer contains phase shifters (see ϕ in close-up). These change the optical path length difference between two paths through the interferometer to change interference and thus change the interferometer effect. These phase shifters are also reconfigurable. A phase shifter is placed on one of the arms in front of each beam splitter. This combination of phase shifters and beam splitters gives enough reconfigurability to change any input distribution into any output distribution. We will refer to the pair of a beam splitter and phase shifter as a node.

2.2 Interferometers with quantum light

These interferometers can also be used in the quantum regime, where the input consists of non-classical states such as single photons. We describe a quantum input of the interferometer in the occupation number

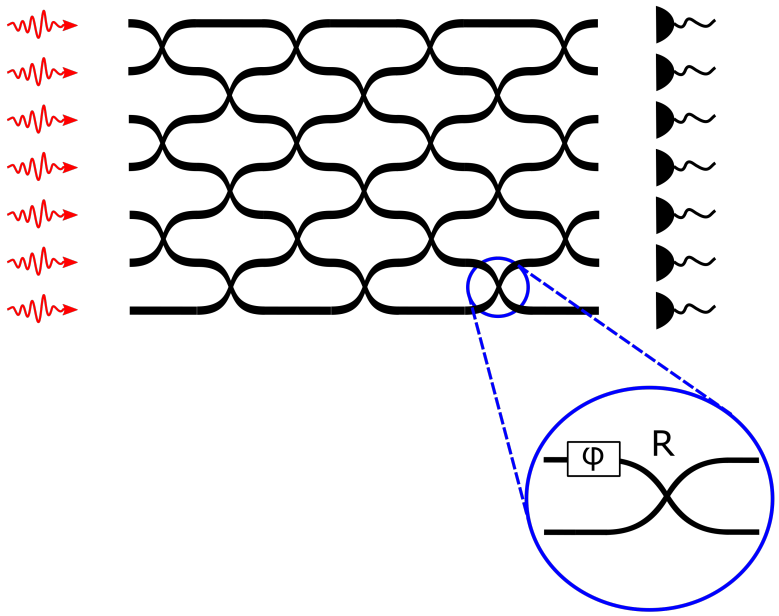

Figure 2.1: *A reconfigurable interferometer. An input distribution of light is inserted into the left and the output distribution is measured at the right.*

picture, $\psi_{in} = |n_1, ..., n_k\rangle$, where n_i indicates the amount of photons in mode i*. Associated with this we then have a set of creation operators: $\hat{\mathbf{a}}^\dagger = (\hat{a}_1^\dagger, ..., \hat{a}_k^\dagger)$.

The working of the interferometer can be described by a unitary matrix U that relates the creation operators of the input modes to the output modes in the following way:

$$\hat{a}_i^\dagger \mapsto \sum_j U_{i,j} \hat{a}_j^\dagger$$

We will demonstrate how this works when the input state has multiple photons. It will become clear photon indistinguishability plays an important role in determining the interferometer output.

We use the simplest example of an interferometer: a 50:50 beam splitter, as displayed in figure 2.2. This beam splitter can be thought of as a 2×2 interferometer described by the following unitary matrix:

$$U = \frac{1}{\sqrt{2}} \begin{pmatrix} 1 & 1 \\ 1 & -1 \end{pmatrix}$$

*By describing the input like this, we have implicitly assumed that our single photons are all indistinguishable: they arrive at the exact same time and have the same wavelength-distribution and polarisation.

Version of March 12, 2017– Created March 12, 2017 - 20:35

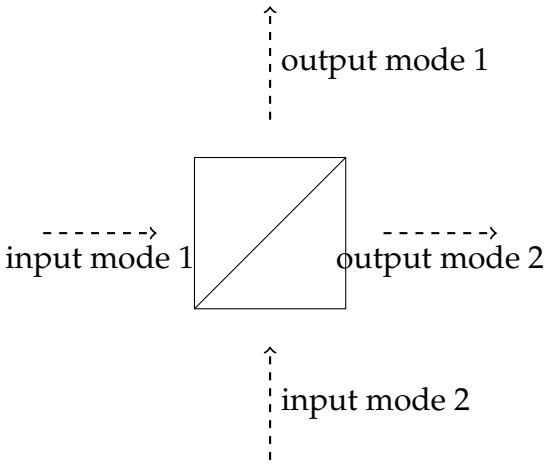

Figure 2.2: *Schematic of a beam splitter*

What happens if two identical photons incident on the two input modes at the same time? In other words, what is the output state for the input $\hat{a}_1^\dagger \hat{a}_2^\dagger |vac\rangle$? Let us calculate:

$$\hat{a}_1^\dagger \hat{a}_2^\dagger |vac\rangle \;\mapsto\; 1/2(\hat{a}_1^\dagger + \hat{a}_2^\dagger)(\hat{a}_1^\dagger - \hat{a}_2^\dagger)|vac\rangle = 1/2(|2\ 0\rangle - |0\ 2\rangle)$$

We see that the outcome is a superposition of both photons being in either one of the modes. Unexpectedly, one will never measure just one foton in one of the output modes. Because the two photons are indistinguishable, the $|1\ 1\rangle$ terms cancelled out. This is called the Hong-Ou-Mandel effect [11]. The operator formalism will take such indistinguishability effects into account for arbitrary interferometer size.

2.3 Applications of photonic interferometers

There has been a lot of interest in these photonic interferometers in the recent years, mostly for use in quantum information technologies [8, 9, 12–14]. We will describe some important applications.

2.3.1 Operations on optical quantum bits

It is possible to encode a qubit using photons in the spatial modes of our interferometers, sometimes referred to as dual-rail logic. Consider one photon that can be in two spatial modes (1 and 2). The general state is then:

$$\alpha|0\rangle_1|1\rangle_2 + \beta|1\rangle_1|0\rangle_2$$

Version of March 12, 2017– Created March 12, 2017 - 20:35

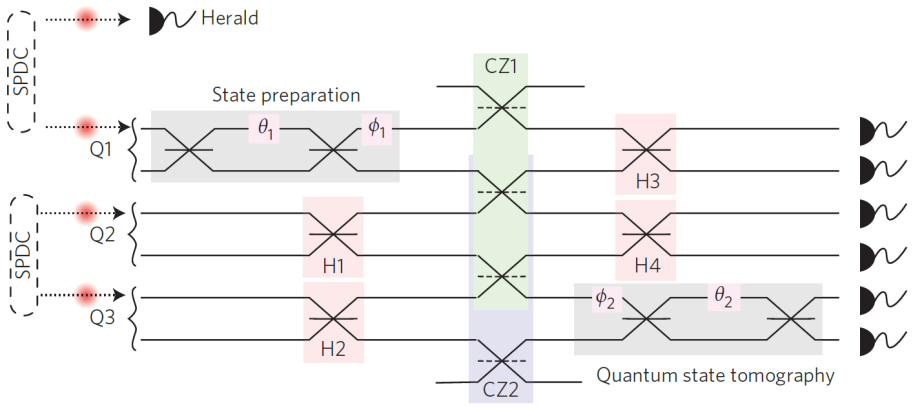

Figure 2.3: *Figure from reference [8] that describes the experimental setup for quantum teleportation.*

The information of one qubit can be incoded into parameters α and β.

One of the applications of a photonic interferometer is to perform quantum teleportation on such a qubit. This has been done experimentally by Metcalf *et al.* [8]. The experimental setup is displayed schematically in 2.3. Three single-photons are produced, inserted into a 6-mode (non-universal) interferometer and detected at the output. This example demonstrates that a three-qubit quantum information protocol can be performed with only a small size reconfigurable interferometer and has, in fact, already been realised.

2.3.2 Boson Sampling

Another quantum information application of interferometers is Boson Sampling. It is a form of quantum computation, but does not make use of qubits.

Although many types of quantum computation have been demonstrated on small scale (e.g. Shor's algorithm [15]), the speed-up of quantum algorithms over their classical counterparts is yet to be demonstrated. To bring us closer to such a demonstration, Aaronson and Arkhipov [16] proposed the Boson Sampling problem. This problem was selected such that it can be solved on an as simple as possible quantum machine, but is still hard to solve classically.

We shall describe the Boson Sampling problem through the quantum experiment it corresponds to. The experiment is depicted in figure 2.4. We

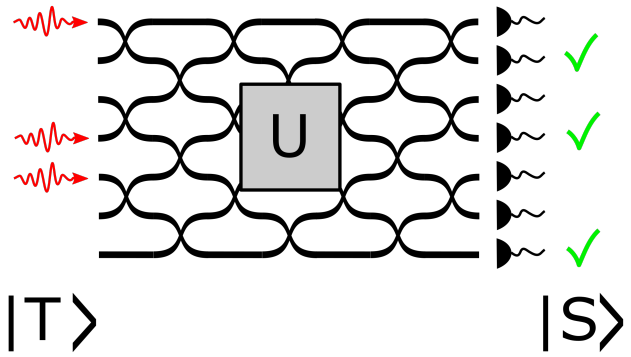

Figure 2.4: *The Boson Sampling experiment. For an input state $|T\rangle$ and interferometer U, a measurement is performed, producing an output state $|S\rangle$.*

need single photon sources, a interferometer, and single photon detectors. We set out sources such that we produce a specific input state $|T\rangle = |t_1, ..., t_k\rangle$, where $t_i \in 0, 1$. We then have an interferometer that performs a known unitary transformation U. At the output, we measure which of our detectors clicks, i.e. we project the output state on the occupation-number basis and obtain a state $|S\rangle$.

This is where the sampling nature of Boson Sampling comes in. Each measurement, we can find a different photon-number output $|S\rangle$, even though the input state $|T\rangle$ is the same each time. We sample from the probability distribution P over the possible photon-number output states, that exists because the output quantum state is in a superposition of different photon-number states. Performing the sampling experiment repeatedly allows us to approximate the probability distribution $P(S|T)$.

Knowing $|T\rangle$ and U also allows us to calculate $P(S|T)$ classically. The corresponding expression is:

$$P(S|T) = \frac{|\mathrm{Per}(U_{S,T})|^2}{s_1!...s_k!t_1!...t_k!},$$

where Per(A) is the permanent of matrix A and $U_{S,T}$ is the matrix produced from U by taking s_i copies of the i^{th} column and t_j copies of the j^{th} row. Aaronson and Arkhipov showed that even approximating such a probability is classically hard, i.e. computation time scales exponentially with the amount of photons. In fact, classical computation is so hard, that for a large number of photons, we expect it to be easier to simply do the

Version of March 12, 2017– Created March 12, 2017 - 20:35

experiment than to do the calculation.

The idea of Boson Sampling is thus the following. Improve current technologies to make Boson Sampling with more photons possible. By comparing experiment runtime to classical computation runtime while increasing the amount of photons, show that quantum computation of Boson Sampling scales better than classical computation. Boson Sampling has been demonstrated with 3 photons by different research groups [8, 9, 13]. The expectation is that Boson Sampling will be able to demonstrate quantum supremacy with less than 50 photons [16].

2.4 Programming a reconfigurable interferometer

An interferometer is called universal if it is capable of implementing any unitary operator by changing the parameters (beam splitter reflectivities and phase shifts) of the interferometer. To be able to do this, the interferometer needs to have an appropriate shape and the right amount of beam splitters. The interferometer in figure 2.1, for example, is universal and can implement any 7×7 unitary matrix.

Reck *et al.* first showed that any unitary transformation can be constructed using only variable beam splitters and phase shifters. They did so by providing an algorithm to determine interferometer parameters from the unitary matrix one wants to implement [17]. The algorithm rewrites the unitary matrix as a product of matrices that each can be identified as a beam splitter and phase shifter node. It decomposes the unitary matrix into smaller pieces and is therefore called the Reck decomposition.

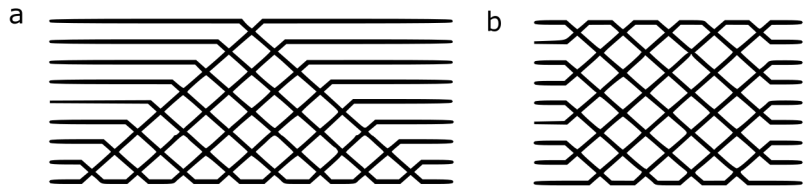

Figure 2.5: ***a****) The design of the interferometer after Reck decomposition.* ***b****) The design after Clements decomposition for the same amount of modes. Figure adapted from [18].*

Recently, a new decomposition algorithm was proposed by Clements *et al.* [18]. Their method is similar to the Reck decomposition, but results

Version of March 12, 2017– Created March 12, 2017 - 20:35

in an interferometer with a different design. The difference between the two types of interferometers is shown in figure 2.5. Here, a universal interferometer with 9 modes is shown for both the Clements and the Reck decomposition.

Both interferometers have the same (minimum) amount of nodes (one beam splitter and one phase shifter): $n(n-1)/2$, where n is the amount of modes. The shape of the Clements interferometer, however, is square, while for the Reck interferometer it is triangular. This means every path through the Clements interferometer is of the same length, while for the Reck interferometer, the path length depends greatly on the path chosen.

Suppose now that each beam splitter has a constant loss: a fixed amount of light is lost when traversing a beam splitter. Most paths through the Reck interferometer now have different loss, while for Clements only the few paths that reach the top or bottom mode have a loss that is slightly different from all the others. For the Reck interferometer, the unbalanced loss affects the output distribution much stronger than for the Clements interferometer, which is thus more reliable in the presence of loss. This is the experimental advantage of using the Clements decomposition over using the Reck decomposition.

2.4.1 The Clements decomposition

We shall now describe the algorithm of the Clements decomposition.

First, we introduce the matrix of a beam splitter with arbitrary reflectivity r^2:

$$\begin{pmatrix} r & t \\ t & -r \end{pmatrix}$$

where we have the constraint $r^2 + t^2 = 1$. A phase shift on one of the two modes of a beam splitter can be desribed as:

$$\begin{pmatrix} e^{i\phi} & 0 \\ 0 & 1 \end{pmatrix}$$

with ϕ the parameter that describes the size of the phase shift. Consider now an interferometer with n modes. The matrix that describes a node

Version of March 12, 2017– Created March 12, 2017 - 20:35

between two neighbouring modes looks like:

$$T_{a,a+1}(\theta,\phi) = \begin{pmatrix} 1 & & \dots & \dots & & 0 \\ & \ddots & & & & \\ \vdots & & e^{i\phi}r & e^{i\phi}t & & \vdots \\ \vdots & & t & -r & & \vdots \\ & & & & \ddots & \\ 0 & & \dots & \dots & & 1 \end{pmatrix}$$

where a indicates the first of the modes that is affected. Note that we always want operations between two physically neighbouring modes to avoid the need for modes to cross-over.

Our goal is to write a unitary matrix U as a product of the above T-matrices, for we can then interpret it as a series of physically realisable nodes. Figure 2.6 depicts this process. We apply $n(n-1)/2$ T-matrices and inverse T-matrices to our unitary matrix by left and right multiplication, respectively. This corresponds to steps 1-5 in the figure. We want each T-matrix to set an element of the product matrix to zero. The values of r and ϕ for the specific T-matrix are fixed by this constraint. The order in which the T-matrices are applied makes sure that, once an element has been set to zero, it will not be changed later on in the algorithm. In the figure, the matrix depicted at each step shows which element is set to zero in which step. The interferometers on the right side show what interferometer node corresponds to the applied T-matrix. By applying T-matrices, we diagonalise the product. A diagonal unitary matrix is physically realisable by phase shifts on all modes. Thus we have related U to a product of matrices that we can actually implement.

To arrive at our final result, we need to rewrite this equation. Besides trivial algebraic operations, we will need to write $T^{-1}D$ as $D'T'$. This is always possible. T' can be determined from T^{-1} by changing ϕ and D' from D by changing the involved diagonal elements. Repeatedly applying this rewriting, we complete the decomposition and arrive at our final equation (step 6 in the figure), that describes U as a interferometer of beam splitters and phase shifters.

Version of March 12, 2017– Created March 12, 2017 - 20:35

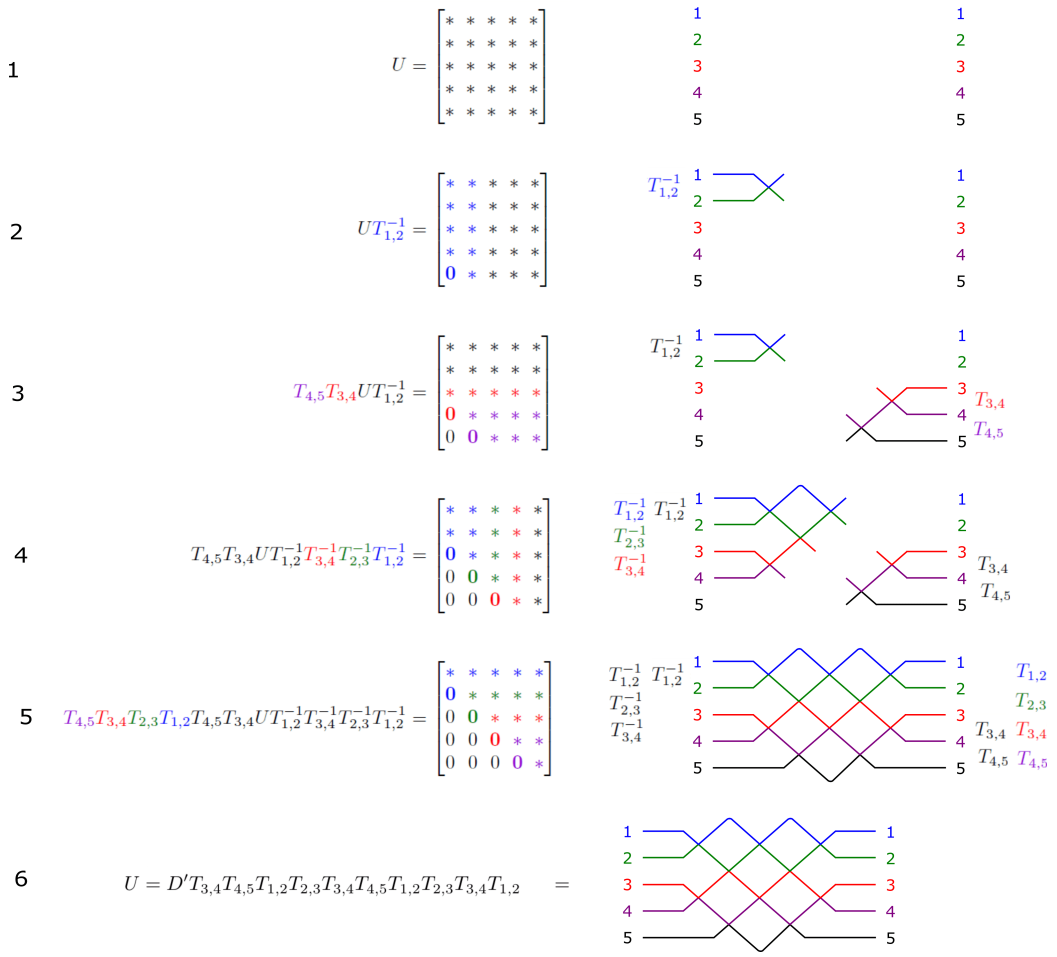

Figure 2.6: *The Clements decomposition algorithm for a 5×5 unitary. The algorithm consists of six steps in this case. The middle column shows the matrix multiplications and the elements of the product matrix that are zero. The right column shows how the T-matrices correspond to interferometer nodes. Figure from [18].*

Chapter 3

Random unitary matrices in realistic multiport interferometers

This chapter describes theoretical research into implementing Haar-random unitary matrices in interferometers. We use the decompositions by Clements et al. [18] and Reck et al. [17] to determine the reflectivities of beam splitters and the phase shifts for these random unitaries. We examine how the distributions of these values scale with the size of the interferometer. After that, we introduce the unbalanced MZIs to see what the effect of imperfections is on the implementation. Finally, we try to mitigate these effects by several techniques.

This work has been written down in the form of a letter-type publication, which is to be sent for peer review shortly after the completion of this thesis. The manuscript of the paper can be found in the next pages and serves as the contents of this chapter.

Scalability of implementing Haar-random unitary matrices in realistic large multiport interferometers

Roel Burgwal,[1] William R. Clements,[1] Devin H. Smith,[2] James C. Gates,[2]
W. Steven Kolthammer,[1] Jelmer J. Renema,[1] and Ian A. Walmsley[1]

[1] *Clarendon Laboratory, Department of Physics, University of Oxford, Oxford OX1 3PU, United Kingdom.*
[2] *Optoelectronics Research Centre, University of Southampton, Southampton SO17 1BJ, UK.*

We investigate implementing Haar-random unitary transformations in multiport interferometers, used in boson sampling. We implement matrices using both the new decomposition by Clements *et al.* and the Reck decomposition. We find that, as the amount of modes increases, lower reflectivity is needed for the beam splitters of the interferometer. A realistic implementation using Mach-Zehnder interferometers is incapable of doing this perfectly and thus has limited fidelity. We show that optimisation of parameters and adding extra beam splitters to the network can help to restore fidelity.

Multiport interferometers are a crucial technology for optical communication and information processing, both in classical and in quantum optics. Classical applications include mode (de)multiplexers for few-mode fibers [1, 2], self-aligning coupling into fiber [3], and spatial-mode and polarisation converters [4]. On-chip multiport interferometers, consisting of an array of reconfigurable beam splitters (BSs) and phase shifters (PSs), are well suited for manipulation of photonic quantum states in e.g. quantum teleportation [5], quantum key distribution [6] or photonic qubit gates [7], due to their inherent phase stability, reconfigurability and ease of fabrication.

One particular quantum-optical task which multiport interferometers are well suited for is boson sampling [8]. The boson sampling task consists of sampling from the output photon number distribution of a large interferometer, which is fed with single-photon inputs. Since the first demonstrations [7, 9–12], many advances have been made, by devising alternative sampling schemes that are easier to implement [13, 14] and by improving the efficiency of single-photon sources [15]. A direct implementation of this task in quantum hardware outperforms simulations on a classical computer for a not unreasonable number of photons, making it a promising technique for an unambiguous demonstration of quantum supremacy.

However, the boson sampling hardness proof both requires that the unitary matrix that describes the interferometer is randomly chosen according to the Haar measure and that the number of modes is much larger than the number of input photons. This has created interest in implementing random unitary matrices in multiport interferometers [16].

In this work, we study the implementation of Haar random unitaries in multiport interferometers with realistic fabrication tolerances. We use a recently developed decomposition algorithm by Clements et al.[17], that implements a unitary transformation in a square array of BS-PS pairs. It can be shown that this decomposition has superior loss tolerance to an older decomposition by Reck *et al.*[18], which uses a triangular arrangement.

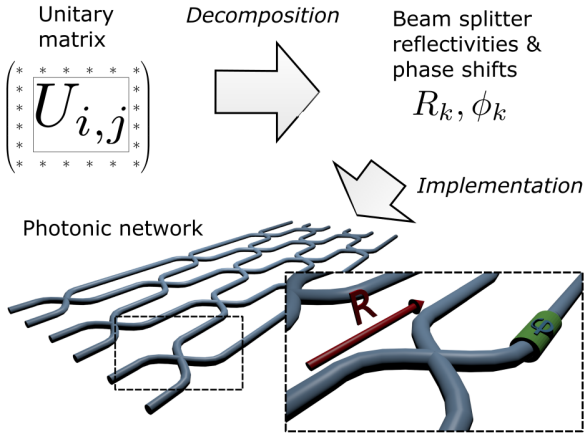

FIG. 1. A unitary matrix can be implemented into a multiport interferometer via a mathematical decomposition. The interferometer consists of pairs of beam splitters and phase shifters (see inset). The decomposition of Clements *et al.* results in the structure of the interferometer shown.

First, we find that the an interferometer implementing random unitary matrices has interesting scaling properties. As the size of the interferom-

eter increases, the majority of the beam splitters take on increasingly low reflectivities. Next, we find that for moderate interferometer sizes (20 modes) and realistic errors in fabrication, neither decompositions can implement any unitary transformation faithfully. Moreover, our results show that the allowable fabrication tolerances decrease with the size of the interferometer, meaning that any level of fabrication tolerance sets a limit on the size of a reconfigurable interferometer.

We also study techniques to mitigate this effect. We find that the interferometer can be made functional again by adding a small degree of redundancy in the form of a few additional layers of BS-PS pairs.

Figure 1 shows the problem under study. We start with a unitary transformation we need to implement. The decomposition algorithms translate the unitary matrix into a set of beam splitter (BS) reflectivities (R_k) and phase shifts (ϕ_k). These can then be implemented in a multiport interferometer, of which each node is a beam splitter and phase shifter pair (see inset).

Our first goal is to understand the what the implementation of random unitary matrices looks like in terms of reflectivities and phase shifts. To do this, we performed the decomposition by Clements et al. on random unitary matrices. We calculated the average reflectivity for every BS in an interferometer of 20 modes, averaging over 5000 random unitary matrices.

Figure 2 shows the spatial distribution of the average reflectivities, what distributions underly these averages and how these scale with the interferometer size.

Figure 2a shows the surprising spatial distribution of average reflectivity. Each grayscale square in the figure represents a beam splitter at the same location in the underlying interferometer, through which light travels from left to right. The modes are labeled along the y-axes and the depth along the x-axes. The colour indicates the average reflectivity, which ranges from 0 to 0.5. It is surprising that the centre of the interferometer has low values of reflectivity. In fact, the majority of beam splitters have low reflectivity and the overall average is 0.18. Note that low reflectivity means most light is transmitted, and thus travels along diagonal lines across the interferometer. Similar results can be found for the Reck decomposition by using the expressions for reflectivity distributions presented in [16].

For figure 2b, we have selected the three regions

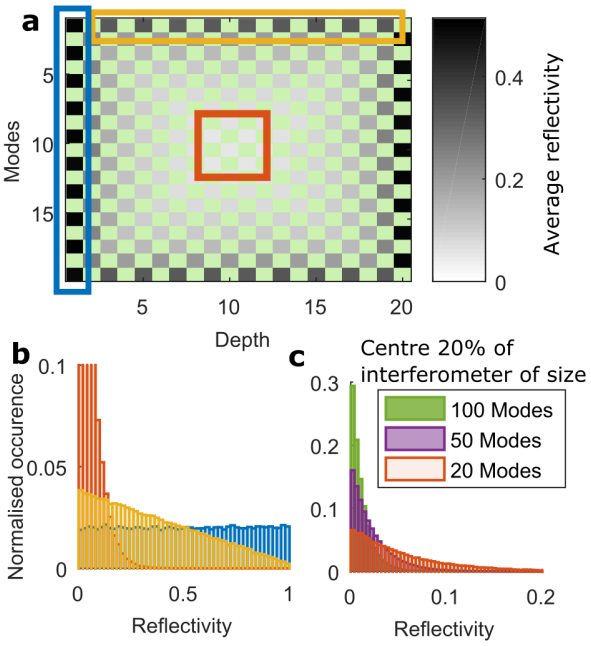

FIG. 2. Interferometers implementing Haar-random unitary matrices show a specific distribution of beam splitter reflectivities. a) shows the spatial distribution of the average reflectivity in a size 20 interferometer. b) Shows the underlying histograms for three regions in the interferometer, the first column, top row and centre. c) shows how the centre-of-interferometer histogram scales with the size of the interferometer. Note the change of scale in c).

from the interferometer which are marked in subfigure a: the first column, top row and the interferometer centre, a square with sides of 20% the interferometer size. For each of these we show the distribution of reflectivity that underlies the average of figure 2a, plotted in their corresponding colours. Most interesting is the distribution for the centre, which is peaked at low values and is zero beyond 0.4.

Figure 2c shows that this effect becomes more pronounced as the size of the interferometer increases. The figure shows how the distribution of the centre of the interferometer changes with interferometer size. We have plotted the corresponding distribution for sizes 20, 50 and 100. The distribution becomes more sharply peaked at low values when increasing size and the average reflectivity becomes lower. Reflectivities above a certain threshold are not found. The distributions for the first column and top row

do not change with size, thus the overall average reflectivity becomes lower as the interferometer size increases. From a similar analysis we found that the Reck decomposition also has this scaling property.

These results can be explained through properties of a Haar-random unitary matrix. Given a matrix U that describes a interferometer, the amount of light that travels from input j to output i in a classical experiment is $|U_{i,j}|^2$. For Haar-random unitaries, the mean L^2-norm of every element is the same, $\langle |U_{i,j}|^2 \rangle = 1/N$. There is only one path, however, light can take from input 1 to output N, on which light is transmitted at each BS (transmission $T = 1 - R$): thus transmission has to be high and, correspondingly, reflectivity has to be low.

To compare the reflectivity distribution of random unitary matrices to those of other interesting interferometer applications, we have also performed the new decomposition on the Fourier transform. The Fourier transform is used in several quantum algorithms, such as Shor's algorithm [19], and is, like Boson Sampling, well-defined for any number of input modes. The resulting reflectivity distribution has low reflectivity on diagonals and high values at the edges. However, the overall average is close to 0.5 and does not strongly scale with size. Thus, the scaling effect for Haar-random unitaries is not present with the Fourier transform .

We now introduce the problem of interferometer imperfections. In particular, we investigate one type of imperfection that stands out when implementing Haar-random unitary matrices. Most reconfigurable realisations of multiport interferometers use Mach-Zehnder interferometers (MZIs) to implement variable beam splitters [7, 10]. These interferometers contain two static 50:50 beam splitters. In practice, these beam splitters are not exactly 50:50, which means the MZI can generally not reflect or transmit all light. As shown above, low reflectivities are needed for the majority of MZIs in a large interferometer implementing random unitaries, thus this is problematic.

We quantified the error resulting from this limitation, using an adapted version of the decomposition. First, we generated a random unitary and decomposed it assuming a perfect interferometer. Next, we modeled the BS error: the reflectivities of the static BSs were drawn from a normal distribution with standard deviation σ and mean 0.5. We refer to σ as the fabrication error. Using these reflectivities, we calculated the minimum and maximum reflectivity of the corresponding MZI. We limited the values determined by the decomposition to these boundaries and constructed the resulting effective unitary. We calculate the fidelity between the effective unitary and the target unitary (see supplementary information) as a measure of similarity.

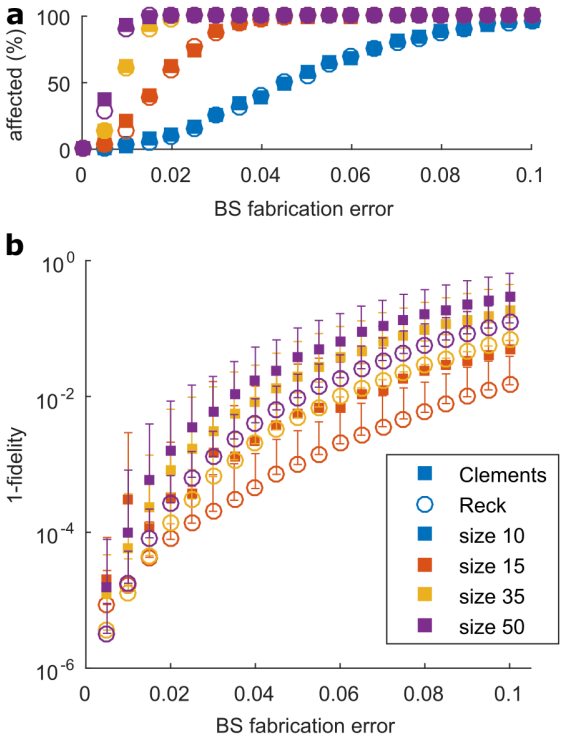

FIG. 3. The effect of unbalanced MZIs on the fidelity of the decompositions as a function of the size of the fabrication error. The Reck decomposition and the decomposition by Clements *et al.* are used for various interferometer dimensions. a) shows us the fraction of the random unitaries that are affected by imperfection. b) shows the fidelity between the target and the effective unitary for the affected matrices when using our adapted version of the decompositions. The error bars show the standard deviation of all data points used in the average.

Figure 3 shows us the effect of the imperfection when using this adapted decomposition. We have performed the adapted decomposition while varying the fabrication error of static BSs, which is displayed on the x-axis. This we have done for various interferometer sizes up to size 50 and for both decompositions.

In figure 3a, we show what fraction of the random unitaries is affected by the error. We see that, for larger interferometer sizes, unbalanced MZIs affect

fidelity for even small fabrication error This means that as MZI multiport interferometers grow in size, they are inevitably affected by the error at some point. The ratio is the same for both decompositions.

Figure 3b shows the average fidelity for those random unitary matrices that cannot be implemented perfectly. The y-axis shows one minus the fidelity, which means that a value of 0 implies the effective unitary is equal to the target. With current state-of-the-art fabrication tolerance (0.025,[20, 21]), we are limited to 0.999 fidelity when building a 50-mode interferometer. To relate this value to experiment, we compare the results of single photon experiments of the effective matrix to the target unitary. We define P^{exp} as the set of single-photon transition probabilities of this implementation and P as the same set for the target unitary. Then, for 0.999 fidelity, $\langle |P_i^{\text{exp}} - P_i| \rangle / \langle P_i \rangle = 0.02$: probabilities are off by 2% on average, with maximum averaging 25%. The Reck interferometer is slightly more robust to these imperfections than the interferometer from the decomposition by Clements *et al.*.

Our adapted decomposition is a first attempt at implementing in an imperfect interferometer, which can be optimised further. To determine whether the fidelity can be improved by fine-tuning the parameters, we have performed numerical optimisation (see supplementary information) with and without added interferometer depth.

Adding depth means adding parameters, giving the interferometer more degrees of freedom than necessary. This extra freedom gives additional room to minimise the effect of limited reflectivity. In our case, we took the interferometer design by Clements *et al.* and added depth by adding columns of nodes, respecting the already present pattern. We used a interferometer of 10 modes and changed depth from 10 to 12, which corresponds to adding 9 BS-PS pairs.

Next, we generated imperfections for these interferometers with a large (0.1) BS fabrication error. We produced random initial configurations. Finally, we generated Haar-random unitary matrices. We then performed the optimisation of the fidelity on the reflectivities and phase shifts of the interferometer.

Figure 4 compares the distribution of 1-fidelity found using the adapted decomposition (blue) to the distribution found after optimisation (red) and after optimisation with extra depth (yellow). Optimisation with normal interferometer depth clearly works

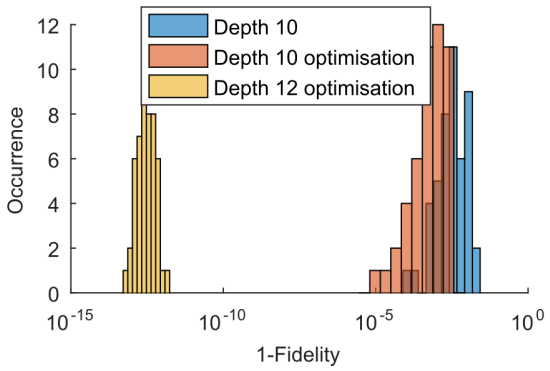

FIG. 4. Numerical optimisation and added depth in a 10-mode interferometer to mitigate the effects of unbalanced MZIs. Figure is a histogram of 1-fidelity for the adapted decomposition (blue) and optimisation with (yellow) and without (red) added depth. The BS fabrication error was 0.1.

to increase fidelity by 1 to 2 orders of magnitude with respect to the adapted decomposition. Next, adding a small amount of depth allows one to increase the fidelity over many more orders of magnitude in all cases. Two added columns already make it possible to achieve near-perfect solutions.

Several other considerations of multiport interferometers with imperfect components can be found in literature. Mower *et al.* [22] performed numerical optimisation of fidelity for interferometer-based quantum gates that suffer from both unbalanced MZIs and unbalanced BS loss. They also increased the fidelity. Miller [23] proposed a scheme to circumvent the effect of unbalanced MZIs by using two imperfect MZIs to implement one perfect variable BS. However, our optimisation results show that this approach is not always optimal, since we obtained near-perfect implementation using depth 12 in a 10 mode interferometer, corresponding to $1.2N$ depth, where the solution by Miller has $2N$. Finally, the scaling of the requirements on interferometer fidelity as a function of the number of photons has been studied [24–26].

In conclusion, we showed that the reflectivities in a multiport interferometer implementing Haar-random unitary matrices are such that fidelities are severely limited by unbalanced Mach-Zehnder Interferometers. We showed that, using optimisation of the parameters, some fidelity can be regained. More importantly, we found that slightly increasing the depth of the interferometer can create near-perfect solutions even in the presence of considerable er-

ror. This approach may also prove useful to mitigate the effects of other types of production imperfections, such as unbalanced loss. The next step is to find a closed-form or low overhead method of finding these settings for a realistic interferometer with added depth. With such a solution in hand, one can greatly increase the fidelity of future large multiport interferometers.

[1] David A. B. Miller. Reconfigurable add-drop multiplexer for spatial modes. *Optics express*, 21(17):20220–20229, 2013.

[2] Daniele Melati, Andrea Alippi, and Andrea Melloni. Reconfigurable photonic integrated mode (de)multiplexer for SDM fiber transmission. *Optics Express*, 24(12):12625, 2016.

[3] David A. B. Miller. Self-aligning universal beam coupler. *Optics express*, 21(5):6360–70, 2013.

[4] David a. B. Miller. Self-configuring universal linear optical component. *Photonics Research*, 1(1):1, 2013.

[5] Benjamin J Metcalf, Justin B Spring, Peter C Humphreys, Nicholas Thomas-peter, Marco Barbieri, W Steven Kolthammer, Xian-min Jin, Nathan K Langford, Dmytro Kundys, James C Gates, Brian J Smith, Peter G R Smith, and Ian a Walmsley. Quantum teleportation on a photonic chip. *Nature Photonics*, 8(10):770–774, 2014.

[6] T Honjo, K Inoue, and H Takahashi. Differential-phase-shift quantum key distribution experiment with a planar light-wave circuit Mach-Zehnder interferometer. *Optics letters*, 29(23):2797–2799, 2004.

[7] Jacques Carolan, Christopher Harrold, Chris Sparrow, Enrique Martín-López, Nicholas J. Russell, Joshua W. Silverstone, Peter J. Shadbolt, Nobuyuki Matsuda, Manabu Oguma, Mikitaka Itoh, Graham D. Marshall, Mark G. Thompson, Jonathan C. F. Matthews, Toshikazu Hashimoto, Jeremy L. O'Brien, and Anthony Laing. Universal linear optics. *Science*, 349(6249):711–716, 2015.

[8] Scott Aaronson and Alex Arkhipov. The Computational Complexity of Linear Optics. *Theory of Computing*, 9(4):143–252, 2013.

[9] Andrea Crespi, Roberto Osellame, Roberta Ramponi, Daniel J. Bord, Ernesto F. Galvão, Nicolò Spagnolo, Chiara Vitelli, Enrico Maiorino, Paolo Mataloni, and Fabio Sciarrino. Integrated multimode interferometers with arbitrary designs for photonic boson sampling. *Nature Photonics*, 7, 2013.

[10] Justin B Spring, Benjamin J Metcalf, Peter C Humphreys, W Steven Kolthammer, Xian-Min Jin, Marco Barbieri, Animesh Datta, Nicholas Thomas-Peter, Nathan K Langford, Dmytro Kundys, James C Gates, Brian J Smith, Peter G R Smith, and Ian a Walmsley. Boson sampling on a photonic chip. *Science (New York, N.Y.)*, 339(6121):798–801, 2013.

[11] Max Tillmann, Borivoje Dakić, René Heilmann, Stefan Nolte, Alexander Szameit, and Philip Walther. Experimental boson sampling. *Nature Photonics*, 7(7):540–544, 2013.

[12] Matthew A. Broome, Alessandro Fedrizzi, Saleh Rahimi-Keshari, Justin Dove, Scott Aaronson, Timothy C. Ralph, and Andrew G. White. Photonic Boson Sampling in a Tunable Circuit. *Science*, 339(February), 2013.

[13] Craig S. Hamilton, Regina Kruse, Linda Sansoni, Sonja Barkhofen, Christine Silberhorn, and Igor Jex. Gaussian Boson Sampling. pages 1–9, 2016.

[14] Marco Bentivegna, Nicolò Spagnolo, Chiara Vitelli, Fulvio Flamini, Niko Viggianiello, Ludovico Latmiral, Paolo Mataloni, Daniel J. Brod, Ernesto F. Galvão, Andrea Crespi, Roberta Ramponi, Roberto Osellame, and Fabio Sciarrino. Experimental scattershot boson sampling. *Science Advances*, 1(3):e1400255, 2015.

[15] Hui Wang, Yu He, Yu-huai Li, Zu-en Su, Bo Li, Heliang Huang, Xing Ding, Ming-cheng Chen, Chang Liu, Jian Qin, and Jin-peng Li. Multi-photon boson-sampling machines beating early classical computers.

[16] Nicholas J. Russell, Jeremy L. O'Brien, and Anthony Laing. Direct dialling of Haar random unitary matrices. *arXiv: 1506.06220*, pages 1–5, 2015.

[17] William R. Clements, Peter C. Humphreys, Benjamin J. Metcalf, W. Steven Kolthammer, and Ian a. Walmsley. An Optimal Design for Universal Multiport Interferometers. (2):8, 2016.

[18] Michael Reck, Anton Zeilinger, Herbert J. Bernstein, and Philip Bertani. Experimental realization of any discrete unitary operator. *Physical Review Letters*, 73(1):58–61, 1994.

[19] P. Shor. Polynomial-Time Algorithms for Prime Factorization and Discrete Logarithms on a Quantum Computer. *SIAM Journal on Computing*, 26(5):1484–1509, 1997.

[20] J. C. Mikkelsen, W. D. Sacher, and J. K. S. Poon. Dimensional variation tolerant silicon-on-insulator directional couplers. *Optics express*, 22(3):3145–3150, 2014.

[21] Dmytro O. Kundys, James C. Gates, Sonali Dasgupta, Corin B E Gawith, and Peter G R Smith. Use of cross-couplers to decrease size of UV written photonic circuits. *IEEE Photonics Technology Letters*, 21(13):947–949, 2009.

[22] Jacob Mower, Nicholas C. Harris, Gregory R. Steinbrecher, Yoav Lahini, and Dirk Englund. High-fidelity quantum state evolution in imperfect photonic integrated circuits. *Physical Review A - Atomic, Molecular, and Optical Physics*, 92(3):1–7, 2015.

[23] Davic A. B. Miller. Perfect optics with imperfect components. *Optica*, 2(8):747–750, 2015.

[24] Anthony Leverrier and Raúl García-Patrón. Analysis of circuit imperfections in BosonSampling. *arXiv*, 0(0):20, 2013.

[25] Gil Kalai and Guy Kindler. Gaussian Noise Sensitivity and BosonSampling. 63(2008477):508–516, 2014.

[26] Alex Arkhipov. Boson Sampling is Robust to Small Errors in the Network Matrix. pages 1–8, 2014.

Chapter 4

Integrated photonics chips

We have described the theory of photonic interferometers, but have said little on how to realise them. In this chapter, we introduce the platform we use to construct interferometers: integrated photonics. The idea is to integrate the waveguides, beam splitters and other optical elements into a silicon chip with a size of the order of centimeters. This method allows for a compact experiment, which in turn allows for good scalability and mass production. Moreover, integrated photonics also provides sub-wavelength stability of path length in the interferometer. This last feature is important when one wants to have controlled interference.

In our experiments, we use integrated photonics chips that are produced by the Planar Optical Materials group from the University of Southampton *. The group is led by prof Peter G.R. Smith.

4.1 Waveguides

The spatial modes of our interferometer are waveguides in the chip. These small tunnels through the silica have a slightly higher refractive index than the surroundings and in that way confine light within them. They have a diameter of about 5 μm and are designed to be single mode at 780 nm.

We shall describe the production process, based on [19]. Fabrication begins with a silicon (Si) waver. On this wafer, three layers of silica (SiO_2) are deposited with a thickness 16,5.6 and 17 μm from bottom to top. The middle layer of silica is doped with germanium, which makes it photosensitive, and with boron, for index matching. The waveguides are

*Optoelectronics Research Centre, University of Southampton, Highfield, Southampton, SO17 1BJ. website: `http://www.orc.soton.ac.uk/pom.html`

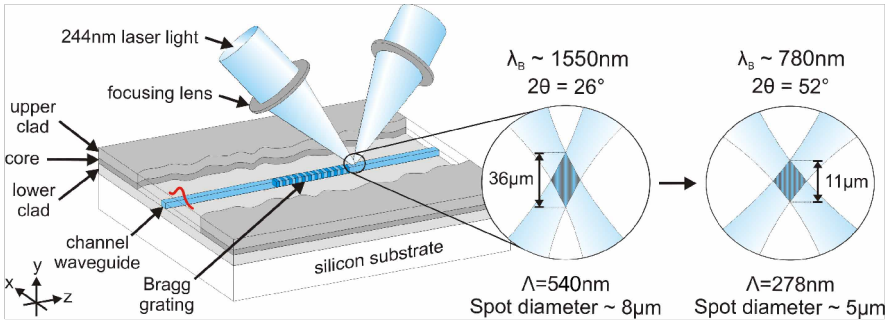

Figure 4.1: *The production process of the integrated photonics chips. A waveguide is written in the middle silica layer by a UV laser. Bragg gratings can be produced through the interference pattern of two laser beams. Figure from [19].*

written in the middle layer using UV light. A 244 nm laser is focussed on the middle silica layer, changing the refractive index permanently.

Figure 4.1 illustrates this process. One laser beam is split in a 50:50 beam splitter and both beams are focussed on the same spot. This small focus area has an interference pattern. When scanning the laser across the silica, the interference pattern is smeared out and the resulting index change is uniform.

Using this interference pattern to do non-uniform illumination, one can create regions of alternating refractive index in the waveguides. These patterns function as Bragg gratings: they reflect a narrow band of light while having high transmission for all other wavelengths. The reflected wavelength depends on the length of the alternating regions. These gratings will prove useful in characterising the on-chip structures, as we will discuss in chapter 5.

50:50 beam splitters can be produced by crossing waveguides at a 2.4° angle [20], which results in a $< 5\%$ error from 50% transmission. This technique is called cross-coupling.

4.2 Mach-Zehnder interferometers as variable beam splitters

To build a multiport interferometer using integrated photonics, we need to construct an on-chip variable beam splitter. This can be done by using a small Mach-Zender Interferometer (MZI) with a variable internal phase

Version of March 12, 2017– Created March 12, 2017 - 20:35

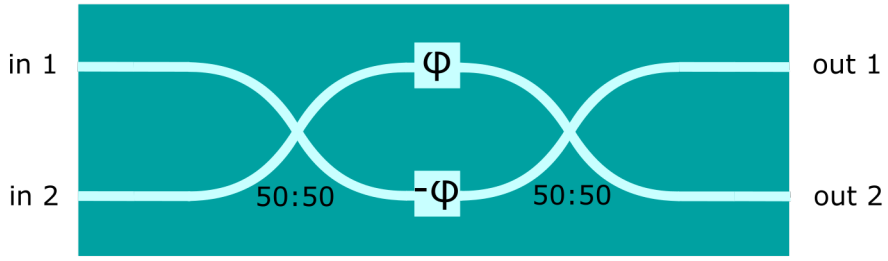

Figure 4.2: *A schematic of a Mach-Zehnder interferometer. It consists of two 50:50 beam splitters and a variable phase shift between the interferometer arms.*

shift, making phase shifters the only variable components we require. A MZI is depicted in figure 4.2. The MZI consists of two fixed 50:50 symmetric beam splitters (cross-couplers), with a pair of phase shifters in between. Because power is distributed between the two heaters, their phase shifts are linked. We model this as phase shifts of ϕ for one and $-\phi$ for the other heater[†]. This model assumes phase shift is linear in the time voltage is applied. We justify this assumption in chapter 5.

We calculate the effect of the MZI from individual components. In matrices:

$$\frac{1}{2}\begin{pmatrix}1 & i\\ i & 1\end{pmatrix}\begin{pmatrix}e^{i\phi} & 0\\ 0 & e^{-i\phi}\end{pmatrix}\begin{pmatrix}1 & i\\ i & 1\end{pmatrix} =$$

$$\frac{1}{2}\begin{pmatrix}e^{i\phi}-e^{-i\phi} & ie^{i\phi}+ie^{-i\phi}\\ ie^{i\phi}+ie^{-i\phi} & -e^{i\phi}+e^{-i\phi}\end{pmatrix} = e^{i\pi/2}\begin{pmatrix}\sin\phi & \cos\phi\\ \cos\phi & -\sin\phi\end{pmatrix}$$

We conclude that the MZI with varying phase shift is a variable beam splitter.

4.3 Variable phase shifters

A local change of waveguide refractive index is used to create a phase difference between two modes. Because photons travel faster through a lower index waveguide, a smaller phase evolution is obtained than when travelling the same distance through higher index material. The change in index is achieved by heating the chip locally with small resistors on top of the waveguides. The resistors are made from NiCr and are about 300 nm

[†]One could object by saying that there is likely to be an offset, leading to phases $\phi+\delta$ and $-\phi+\gamma$, where δ,γ are constants. In the appendix, we show that these offsets do not affect results presented here

Version of March 12, 2017– Created March 12, 2017 - 20:35

thick and 2 mm in length along the waveguides. The target resistance is $1.8k\Omega$. The wiring leading to the resistors is made of gold.

A heater is placed on both arms inside each MZI and on both arms before each MZI to construct a variable beam splitter and phase shifter. A custom made circuit board with field-programmable gate arrays (FPGAs) is used to control the heaters. A voltage ranging between 15 and 20 V is quickly alternated between the two resistors in a pair (one pair inside the MZI, one in front). The distribution of voltage can be set in 256 steps, where 1 means voltage is always applied to one resistor and 256 means voltage is always applied to the other resistor.

Alternating between a pair of heaters has an important advantage over variable voltage on a single heater. The total amount of heat dissipated in each pair remains constant, whereas a single heater would have varying heat production. When using pairs of heaters, the heat production on the chip remains the same, regardless of phase shifter settings, allowing for less cross-talk between different pairs of heaters and also reducing the time the chip takes to thermalise after changing heater settings.

4.4 Modular chip architecture

The Southampton chip design has a unique feature: interferometers are produced in segments, called modules. Figure 4.3a shows the schematic single module. A module has a number of input (bottom) and output (top) modes. The module contains one row of MZIs, in this case there are only two. The MZIs couple modes pairwise. On both sides of the MZIs, straight waveguides are added for testing purposes. As described earlier, each MZI has two pairs of phase shifters. In the figure, the wiring and heaters on top of the chip are depicted in gold. The tapered regions of the wiring are the heaters. The wiring ends in contacts, that are wirebonded to external electronics that supply and regulate the power.

Figure 4.3b shows a picture of actual modular chips. These chips have 24 modes. 4 modes are straight waveguides (two on each extreme of the chip). The other 20 modes are coupled pairwise by 10 MZIs. The silica-on-silicon chips are the dark grey squares in the centre. The blue wings contain contacts that are on the one hand wirebonded to the on-chip wiring whilst on the other hand can be connected to by ribbon cable.

The modular chips are connected together in the following way. Individual modules are connected head-to-tail, by coupling the output modes of one chip into the input modes of another. Each second chip is offset by one mode. Figure 4.4 gives an example of this coupling for three chips.

Version of March 12, 2017– Created March 12, 2017 - 20:35

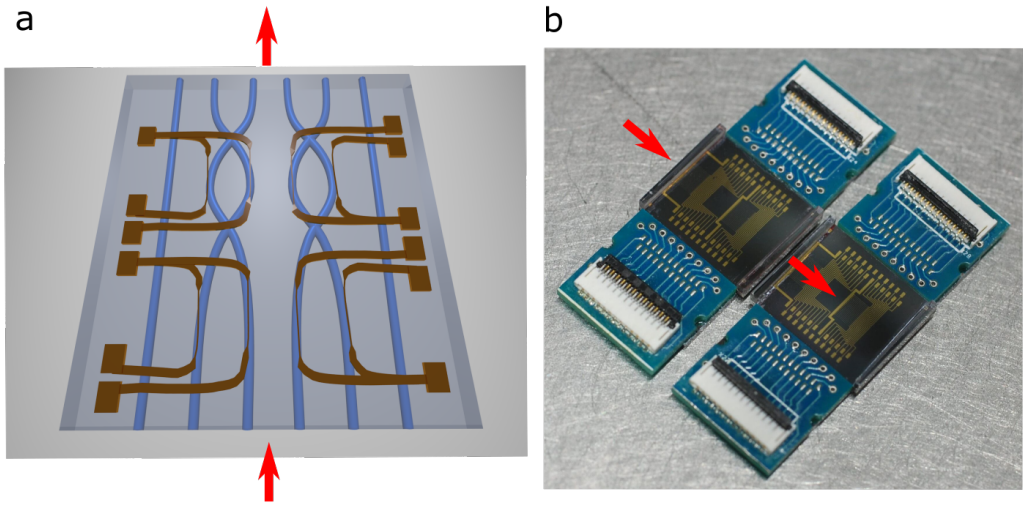

Figure 4.3: *The Southampton modular chips. a) A schematic of the chip, with straight waveguides and Mach-Zehnder interferometers with heaters on top (gold). b) A picture of two actual modular chips. Gold wiring is visible on top, waveguides are not visible. Red arrows indicate direction of light in both figures.*

Wiring was left out for convenience. Offsetting by one mode allows one to create an interferometer in which each input mode couples to each output mode. In the resulting assembly, one can isolate an interferometer according to the design by Clements et al. or Reck et al. For example, by setting the bottom MZI of the middle chip in figure 4.4 to full reflectivity, the top three input and output modes are connected by a universal multiport interferometer that can implement any 3×3 unitary transformation.

The modular structure was introduced by Southampton to optimise the quality of the integrated photonics chips. Because of the way the production process works, it is beneficial to produce interferometers in segments, called modules, that are each made in a separate silicon chip. There are, however, other advantages to this design. The modular architecture allows one to access and characterise the individual components (cross-couplers, heaters), before assembling the interferometer. Malfunctioning components can be excluded easily by replacing a module. Moreover, interferometers of different depth and structure can be made using the same components.

Version of March 12, 2017– Created March 12, 2017 - 20:35

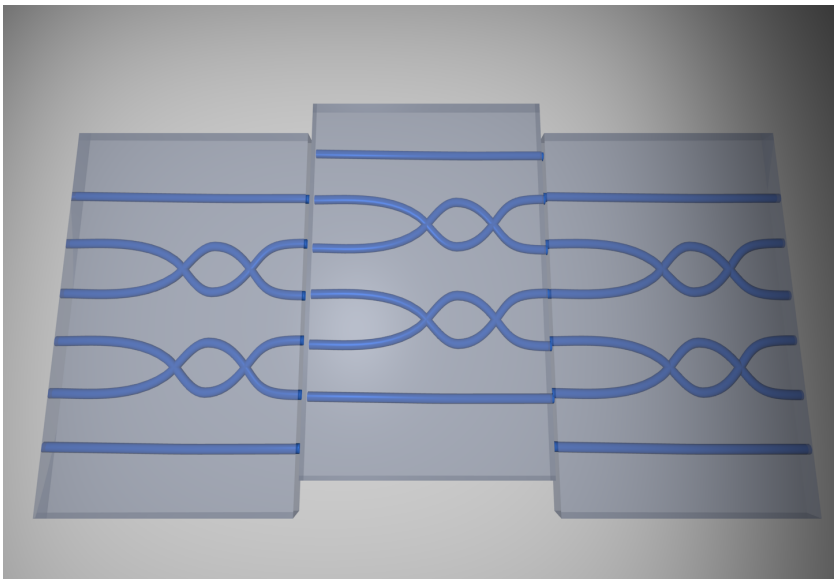

Figure 4.4: *An example of a three-chip assembly. This assembly contains several universal 3-mode interferometers. Chip heaters were left out in this figure for convenience.*

Version of March 12, 2017– Created March 12, 2017 - 20:35

Chapter 5

Modular chip experiments

In this chapter, we report experimental testing of Southampton integrated photonics chips. First, we characterised several properties of the modular chips. These include transmission, propagation loss, cross-coupler reflectivity and MZI reflectivity tuning. Indications of the losses are important because the efficiency of photon sources, and as a consequence, chip losses, are the limiting factors for many-photon experiments. We describe the set-up used to couple from fibre into chip and explain techniques used to determine these characteristics. Second, we assembled three modular chips into a larger interferometer. We describe the assembly and perform overall transmission measurements.

5.1 Experimental Set-up

During both single-module and chip assembly experiments, we use the set-up in figure 5.1. First, as a source of light, we use a super-luminescent light emitting diode (SLED), that produces broadband light centred around 780 nm with 40 nm bandwidth. The output intensity is about 1 mW. A broadband source is used to be able to measure reflection from Bragg gratings with a different wavelength using the same light source. Light is constrained to polarisation maintaining single-mode fibres in the set-up.

First, light travels through a 50:50 fiber beam splitter. One output is terminated and back reflections are stopped. The other output is connected to one of our switches. These are mechanical switches that allow for fast, computer controlled switching of one input channel to 16 output channels. These switches do have channel-dependent loss. We measured these losses and corrected measurements accordingly.

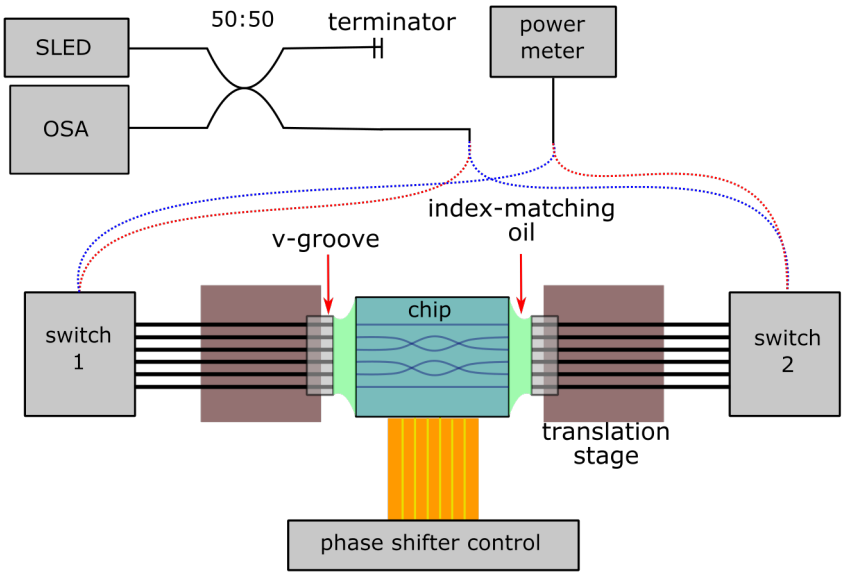

Figure 5.1: *The set-up used to characterise individual chip modules.*

The 16 outputs of this switch are connected to a v-groove array. This device has 16 normal fibre inputs. It arranges the cores of these fibres in a small block, in which they are evenly spaced, separated by 80 μm. The waveguides on-chip are spaced in the exact same way. The v-groove array can thus be used to couple the fibres into the chips waveguides. The array is polarisation-preserving. To couple light into the chip, the v-groove face and the chip face need to be aligned with micrometer precision. To this end, we use a ThorLabs NanoMax 600 translation stage (purple in figure) to hold the v-groove, while the chip rests on an independent support. The stage has 6 degrees of freedom, allowing us to align the two faces in both position and orientation. Coupling is optimised manually using feedback from continuous transmission measurements. In optimal alignment, the two faces almost touch. We apply an index-matching oil between the faces to maximise coupling. Also, to control the chip, we are electronically connected to the on-chip heaters.

Light couples out of the chip again, using another v-groove on an identical translation stage. Using a second switch, we can couple any of these 16 outputs into one output fibre. This light is used to perform power measurements. Some light is reflected back by the Bragg gratings on-chip. This light returns through the switch to the beam splitter. Here, part of it is sent to the additional input mode. Here, we have connected an Optical Spectrum Analyser (OSA), which we use to measure the spectrum of the

Version of March 12, 2017– Created March 12, 2017 - 20:35

reflected light.

As mentioned in the previous section, we need to perform measurements from both sides of the chip. To this end, we switch connections between the beam splitter and the switches and the power meter and switches (red,blue, dotted lines). By doing this, we reverse the direction of light through the chip without decoupling.

5.2 Bragg grating-based measurement techniques

In this section, we describe two techniques that make use of the Bragg gratings in waveguides to determine propagation loss and cross-coupler reflectivity.

5.2.1 Propagation loss

An elegant technique to determine propagation loss in waveguides has been invented by Southampton [21]. Our straight waveguides each contain several Bragg gratings that are spread out over the length of the waveguide. This is shown in figure 5.2a. These gratings have a detectable reflection for only a narrow band of wavelengths. The different gratings work at different wavelengths. We send broadband light into the waveguide and measure the spectrum of the back reflected light.

Measuring the reflection from both sides of the waveguide allows one to find the loss. An example of the measured spectra is found in figure 5.2b. As is shown in [21], one can find the loss by performing a linear fit to this data:

$$\ln\left(\frac{R_i'}{R_i''}\right) = C - 0.92\gamma x_i \tag{5.1}$$

Where R_i' is the power of the reflection from the Bragg grating at position x_i, R_i'' is the power of the same reflection but now measured from the other side of the waveguide, C is a constant and γ is the propagation loss in dB/cm. A good property of this method is that it is insensitive to the coupling loss at either side of the waveguide.

We perform reflection measurements and use the area of peaks in the reflection spectrum as the power of reflections. We plot the log ratio of equation 5.1 as a function or position in the waveguide. We apply a linear fit to this data, an example of which can be seen in figure 5.2c, and extract the propagation loss.

Version of March 12, 2017– Created March 12, 2017 - 20:35

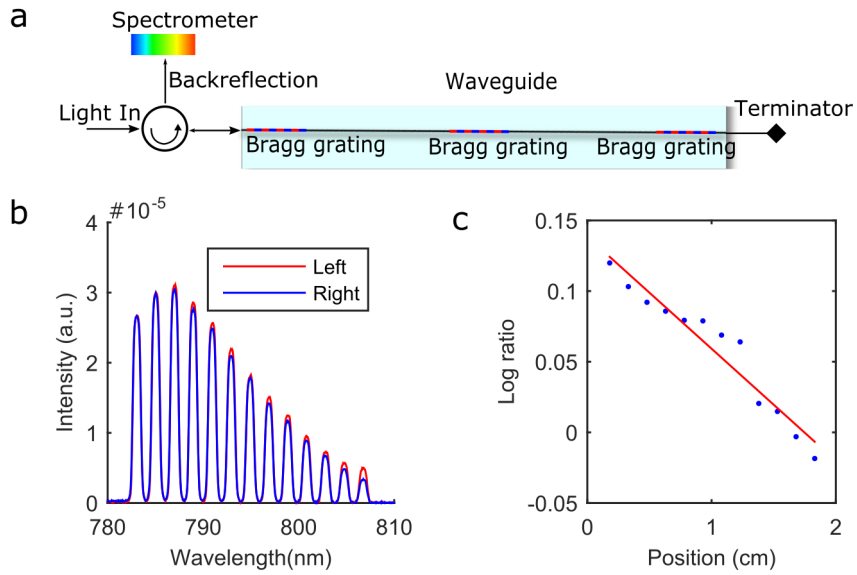

Figure 5.2: ***a)*** *Schematic of the measurement technique for propagation loss. Figure adapted from [22].* ***b)*** *An example of the spectrum of light reflected in a straight waveguide. In this case, there were 13 Bragg gratings.* ***c)*** *The log ratio (equation 5.1) as a function of position along the waveguide. Red line is a linear fit from which we retrieve the propagation loss.*

5.2.2 Cross-coupler reflectivity

Bragg gratings can also be exploited to determine the static reflectivity of the MZI cross-couplers. The MZIs are produced with six Bragg gratings each, as depicted in figure 5.3. The reflectivities of the gratings are labelled r_i and the reflectivities of the two beam splitters are labelled η. All gratings again work at different wavelengths.

Let us consider the back reflection of light entering from input 1, reflected off grating 2 and measured again at input 1. We call this quantity $R_{1,2}$. We set the input power to unity for simplicity. The power of the reflection can then be expressed in the following way:

$$R_{1,2} = s_1 l_{1,2}^2 \eta_1^2 r_2$$

Where s_1 is the combined in and out coupling loss at input 1 and $l_{1,2}$ is the transmission loss between input 1 and grating 2. Similarly, we have:

$$R_{1,5} = s_1 l_{1,5}^2 (1-\eta_1)^2 r_5, \quad R_{2,2} = s_2 l_{2,2}^2 (1-\eta_1)^2 r_2, \quad R_{2,5} = s_2 l_{2,5}^2 \eta_1^2 r_5,$$

Version of March 12, 2017– Created March 12, 2017 - 20:35

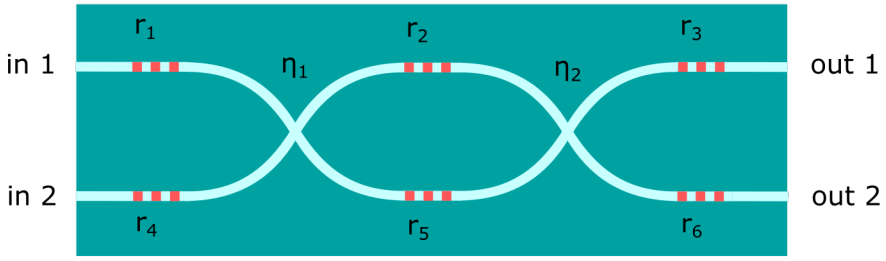

Figure 5.3: *A Mach-Zender interferometer with Bragg gratings as constructed in our chips.*

We can then produce the ratio:

$$\frac{R_{1,2}R_{2,5}}{R_{1,5}R_{2,2}} = \frac{l_{1,2}^2 l_{2,5}^2 \eta_1^4}{l_{1,5}^2 l_{2,2}^2 (1-\eta_1)^4}$$

We then assume losses are distributed symmetrically, i.e. $l_{1,2} = l_{1,5} = l_{2,2} = l_{2,5}$, and we find:

$$R = \frac{R_{1,2}R_{2,5}}{R_{1,5}R_{2,2}} = \frac{\eta_1^4}{(1-\eta_1)^4}$$

or

$$\eta_1 = \frac{1}{R^{-1/4}+1}$$

Thus we can determine cross-coupler reflectivity independent of fibre-chip coupling efficiency. The reflectivity of the second beam splitter can be obtained in the same way using reflections from the other side.

5.3 Modular chip characterisation

The following section contains the results we obtained from three modular chips using the set-up and techniques described in the previous two sections.

5.3.1 Losses

We determined the amount of light that is transmitted in a chip experiment. For straight waveguides, losses are caused by both propagation loss inside the chip and coupling in and out of the chip. Transmissions for

Version of March 12, 2017– Created March 12, 2017 - 20:35

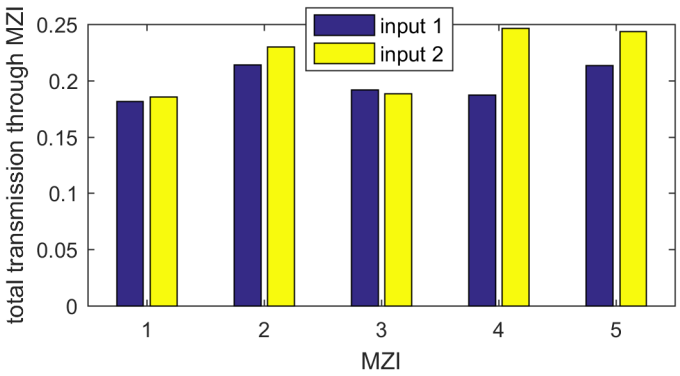

Figure 5.4: *The MZI transmission when illuminating one input arm for five neighbouring MZIs on one of the modular chips.*

straight waveguides are in figure . The best figure we obtained is a 71% transmission of power.

An example of typical transmissions for MZIs is displayed in figure 5.4. Light was sent into either one of the inputs of a MZI. We then measured the sum of the intensities at both outputs, from which we determine the total transmission. MZI transmission is lower than straight waveguide transmission, at an average of about 20%. We believe there are two reasons for this: first, bent waveguides are more lossy than straight ones and second, loss occurs at cross-couplers. Loss is not constant across different MZIs. Unbalanced loss has been shown to be a source of error in photonic networks [23]. Surprisingly, loss through both inputs of a MZI is also not always the same. This points to either a large difference in coupling efficiency at the two inputs, or asymmetric loss at the cross-couplers. A next step in analysing the modular chips would thus be to determine whether differences in transmission are due to coupling differences or cross-coupler losses, as this indicates what aspect needs to be improved the most.

We have determined propagation loss in the straight waveguides on the modular chips. The reflections from the Bragg gratings have a low intensity and can easily be distorted by other reflections in the system. Therefore, we have only been able to measure reflection spectra of sufficient quality for half the straight waveguides on the modular chips. The results are in figure 5.5. The value in parentheses is the upper limit of the 95% confidence interval.

The propagation losses we found are similar to value of 0.23 dB/cm found by collaborators in Southampton using the same writing and measuring techniques, only at 1550 nm[21]. The differences in propagation

Version of March 12, 2017– Created March 12, 2017 - 20:35

Loss(dB/cm)	Transmission(0-1)
0.24(0.44)	0.48
0.47(0.69)	0.29
0.39(0.74)	0.49
0.56(1.04)	0.48
0.27(0.47)	0.71
0.24(0.31)	0.52

Figure 5.5: *Total transmission and propagation loss of six different straight waveguides.*

loss are not big enough to explain the difference in transmission. A 1 dB/cm propagation loss still means only 20% of power is lost in the chip. Thus it is likely that differences in transmission are due to different couplings.

Having measured the propagation loss and total loss independently, we can estimate coupling loss. We remove the propagation loss over 1 cm of chip from the total transmission. We find:

$$\sqrt{\frac{0.71}{10^{-0.27/10}}} = 0.87$$

in other words, we have an estimated most efficient coupling of 87% at the chip to v-groove interface.

5.3.2 Reflectivities of beam splitters

For the three modular chips, we have collected data on the reflectivities of cross-couplers. Out of 60 couplers ($3 \times 10 \times 2$), we have successfully determined the reflectivity for 44. In other cases, other reflections in our set-up made distinguishing the grating reflections impossible. The results are presented in figure 5.6. The data of first (outside the MZI) and second (inside the MZI) beam splitters are separated, because they appear to follow different distributions.

First, the values of reflectivity are too high and range from 0.5 to 0.64. The fact that no reflectivity values of under 0.5 are found suggests that the main cause is not an uncertainty in the crossing angle: if that were the case, you would also expect to find values below 0.5. The values we found differ from those found by collaborators [20]. Their values also contain ratios below 50% and are limited in error to $\pm 5\%$. It is possible that we have made wrong assumptions in our calculations. We have assumed

Version of March 12, 2017– Created March 12, 2017 - 20:35

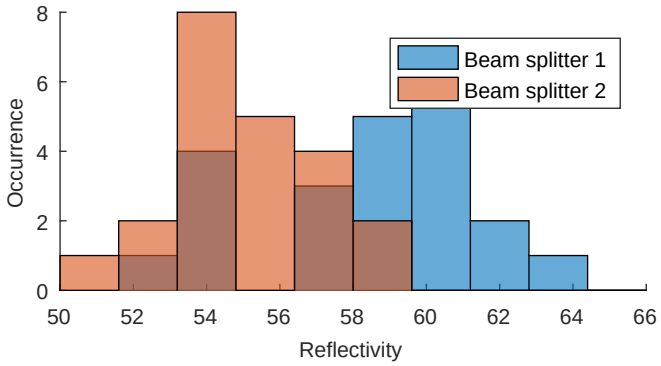

Figure 5.6: *Histogram of cross-coupler reflectivities from modular chips.*

symmetry of the MZI in that losses in different paths are the same, which could be false.

Second, the results for the first BS are generally higher than for the second BS. Both of these findings are important feedback for the chip production group.

5.3.3 Phase shifters

We tested all the MZIs on the modular chips to determine the function of the phase shifters that are inside the MZIs. We illuminate one input port of a MZI. By measuring the intensity at both outputs of the MZI while scanning through the heater settings, we perform a characterisation.

Figure 5.7 shows an example of the measurement results for one MZI. Intensity at output 1 and 2 is plotted against settings (red, blue, filled markers). We have successfully fitted the data with a $\sin^2$ function, indicating that phase shift is a linear function of the heater setting. In contrast with what we expect, we do not reach full extinction in either of the output arms. The lowest transmission we obtain can not be explained by the measured values of cross-coupler reflectivity.

The green data in the figure is the sum of both output intensities for the measurement with both phase shifters. Surprisingly, it is not constant. The green line is the mean value and helps to illustrate this fact. The loss in the MZI is thus dependent on the phase between the two arms. This behaviour can be modelled by assuming the cross-coupler couples not two, but three modes. The added mode is a loss mode. Such a model gives exactly the phase-dependent loss we are seeing, thus suggesting there is a third mode in which light can couple. This also helps explain the fact that intensity in a single output does not reach 0 for any phase shift.

Version of March 12, 2017– Created March 12, 2017 - 20:35

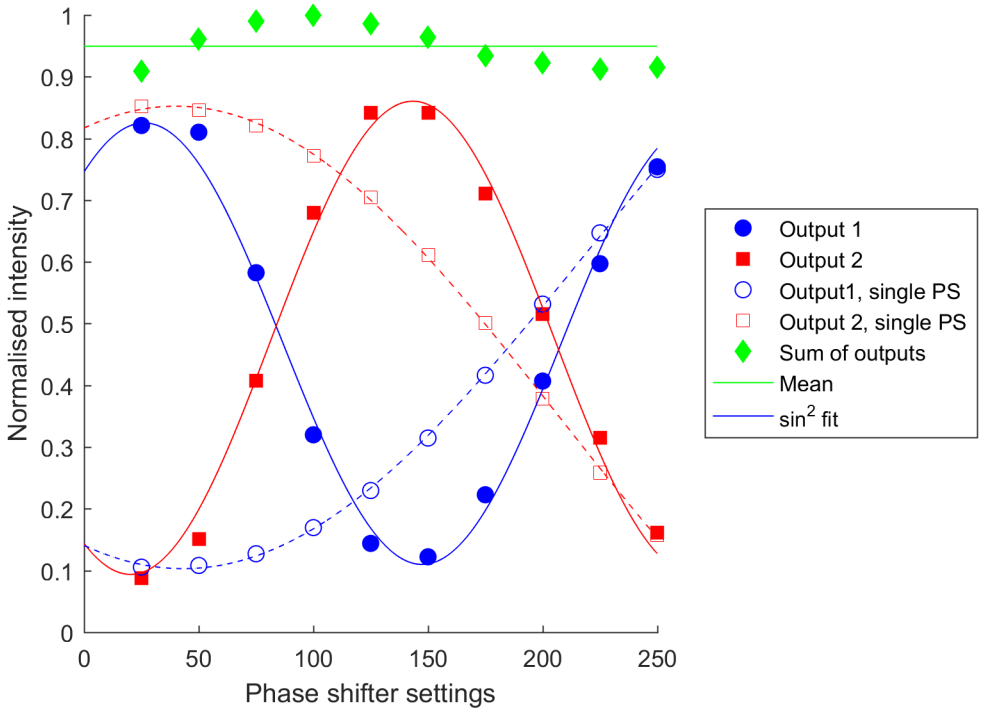

Figure 5.7: *The effect of phase shift on the transmission of a MZI. For illumination of a single input, intensity at both arms (red, blue, markers) is measured while varying heater settings. We use both the heater pairs (filled markers), as well as single heaters (open markers). Green data (line is average of data) shows the total transmission of intensity as a function of setting for the heater pair.*

In figure 5.7, the empty red and blue markers show single phase shifter data. To produce this data, we use only one phase shifter of each pair. As a result, reflectivity changes more slowly when changing the settings.

The results we have presented here show what the chip design is capable of. In practice, however, many phase shifters do not yet function optimally. The reflectivity range is too limited for most phase shifters, because heater resistance is often higher than intended.

5.3.4 Interferometer arm length difference

Transmission spectra from the MZIs can give information about the path length difference between the two arms of the interferometer. Consider a MZI of which the lengths of the arms differ by ΔL. Wavelength-dependent transmission through the interferometer should then be $\propto \cos^2\left(\frac{2\pi\Delta L}{\lambda}\right)$.

We also model a wave-length independent loss by setting a transmission factor α. Altogether:

$$T(\lambda) = \alpha \cos^2\left(\frac{2\pi\Delta L}{\lambda}\right) I(\lambda),$$

where T is transmission and I is the input spectrum. We measured the spectrum of SLED light after it travelled through a MZI of a chip module. We calculated the ratio T/I, which we expect to follow the $\cos^2$ pattern if path length difference is not very small. We find that the $\cos^2$ is not present in the data. We estimate that the argument of the $\cos^2$ has to change less than $\pi/4$ for this effect to not be noticeable. This leads us to the conclusion that the arm length difference is less than 2 μm.

5.4 Experiments with a three-module assembly

In this section, we describe how we coupled three modular chips together and performed transmission measurements on this assembly.

5.4.1 The process of assembly

We will describe the process we used to assemble the chips. The starting point is the setup described in chapter 5, with a single modular chip coupled to both v-grooves.

First, we make sure the chip and v-grooves are aligned optimally. Then, we remove the index-matching oil on one side of the chip and replace it with UV-hardening optical glue. This glue does not harden until illuminated by strong UV-light, allowing us to perform last-minute optimisation of the alignment. Furthermore, the glue matches in index to improve coupling efficiency. We attach one v-groove to the chip in this way. The chip with attached v-groove is then placed on the translation stage. A new chip can then be placed on the support between the translation stages and process is repeated, now gluing chip-to-chip. Finally, the other v-groove is glued to the chip-assembly and the process is complete.

Using this process, we made an assembly of three modular chips that is displayed in figure 5.8. Subfigure a is a picture of the actual chips, connected to the v-grooves on both sides. Subfigure b shows a schematic of the assembly, where again we have reduced the amount of MZIs from 10 to 4 for convenience.

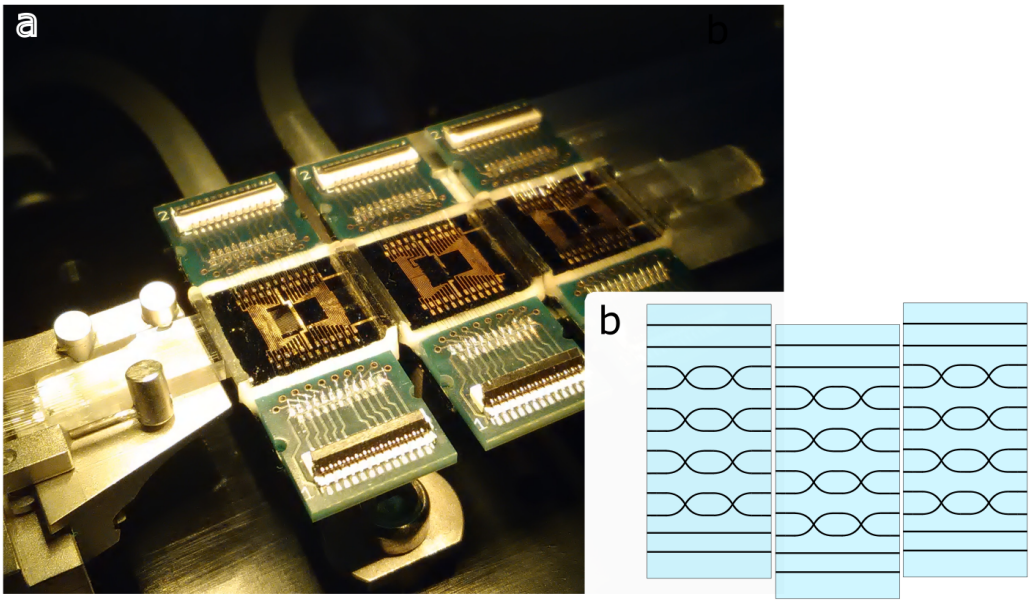

Figure 5.8: *The chip assembly. a) Picture of the assembly in setup. b) A schematic of the resulting network (depicted with a reduced amount of modes).*

5.4.2 Transmission through the interferometer

We measured the transmission of this assembly. We corrected for losses in our set-up and thus present here the transmission from fibre-to-fibre, through the chip. The results are in figure 5.9. We inserted light into a certain input and summed over the intensity at all outputs. We measured two inputs that have a straight waveguide path to the output and 10 inputs that travels through MZIs. We reach at most 39% transmission for straight waveguides. Values are similar for both of these, even though they are positioned at opposite sides of the chip. This seems to indicate alignment between chips is good for all modes. Transmission for the MZIs paths is lower, at on average 5%.

We compare this value to other experiments. One of the highest transmissions is by Carolan et al., who report an average 58% transmission fibre-to-fibre of their 6-mode Reck design interferometer [9]. Our assembly is expected to have $< 1\%$ transmission for a 6-mode interferometer according to the Clements et al. design. To match the state-of-the-art in terms of transmission, the on-chip and coupling losses will have to be strongly reduced.

Version of March 12, 2017– Created March 12, 2017 - 20:35

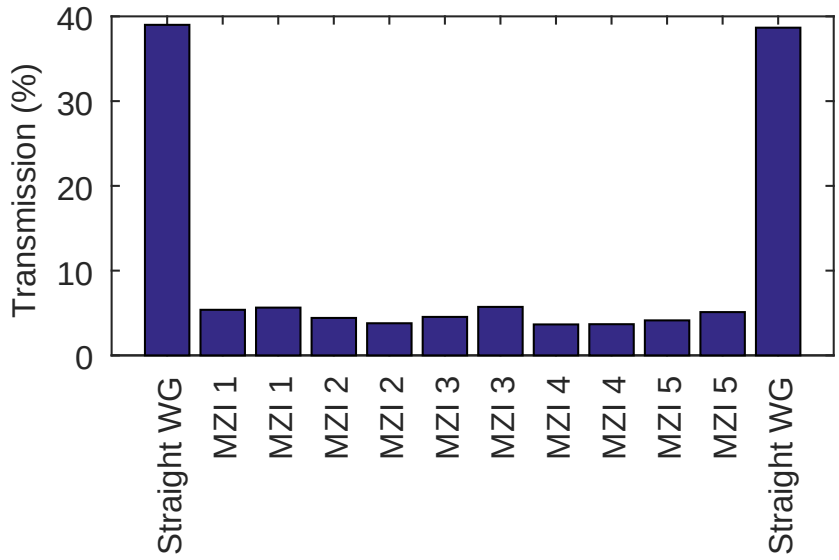

Figure 5.9: *Transmission of power through the three-chip assembly. Data is presented for two paths through straight waveguides and 10 paths that run through MZIs.*

5.4.3 The experimental challenge of assembly

Although the modular architecture makes for, among other benefits, higher quality chips, it also has downsides. First, a chip-to-chip coupling efficiency of about 90% causes a rapid decrease of transmission with the amount of modules. To create a universal interferometer, the amount of modules has to be at least equal to the amount of modes and thus many modules would have to be connected to build a large interferometer. To make this possible, coupling efficiency will have to be increased. Second, to ensure optimal coupling, sub-micrometer precision and stability is needed. This is difficult to obtain with the manually operated translation stage and for further optimisation it may be necessary to control translation using a piezo motor. Finally, gluing the components together makes the assembly fragile, making the process of manually connecting many modules challenging.

Version of March 12, 2017– Created March 12, 2017 - 20:35

Chapter 6

Outlook

In this chapter, we first suggest several steps that can be taken in the next few months to further the research. After that, we discuss changes that can be made on a longer (1 year+) time-scale.

As we demonstrated in the previous chapter, losses are the most prominent issue with the Southampton chips. To reduce loss, the working of cross-couplers needs to be thoroughly understood. A starting point would be to produce new chips with MZIs with varying parameters. For example, changing the cross-coupler angle and measuring coupling into the suspected third mode could provide clues to the nature of this additional mode. The same could hold for varying waveguide diameter or UV-writing beam intensity. Additionally, Kundys *et al.* [20] show that cross-coupling at $\approx 1^\circ$ (instead of 2.4°) also results in a 50:50 beam splitter, which could have lower loss.

Regarding the heaters, there are some questions as to whether the heater resistance changes over time when used frequently. The total heat production of all resistors on a single module is considerable and this can possibly result in structural changes to the resistors over time. Although not properly documented, it has been observed that applying 30 V to the resistors can change their resistance in a matter of seconds. Therefore, we recommend resistance-versus-time measurements on modular chips. Also, it is not clear how strongly adjacent MZIs influence each other. Heaters from one MZI heat an adjacent MZI and therefore influence the reflectivity. One idea would be to test MZI reflectivity while varying neighbouring heater settings.

From the experiments presented in the previous chapter, we draw several conclusions about the long term development of the integrated photonics chips.

In this report, we have demonstrated that the Southampton design for phase shifters is capable of full tunability. However, only a small fraction of heaters has the correct resistance and most of the time, the range is limited. Thus, the challenge that remains is creating a production process that creates a more consistent product.

We have also addressed the issues that arise from the assembly step. Producing the interferometer in segments adds room for imperfections because segments have to align and be stable with sub-micrometer precision. With the current chips and assembly technique, building a 20-mode interferometer (the maximum number of modes with just one parallel module) with low loss is not possible. Therefore, somewhere in the near future, changing the chip writing process to produce monolithic chips would solve a lot of problems.

If the cross-couplers cannot be improved, they can possibly be replaced by evanescent couplers, that have also been demonstrated in integrated photonics [13, 24].

Finally, on-chip photon sources [25] and detectors [26] are being developed. These make it possible to perform an entire experiment in integrated photonics and would thus remove the necessity to couple in and out of the chip, reducing losses.

Chapter 7

Conclusion

*Multiport interferometers are a technology whose development is well under way and that will serve in many different applications. Integrated photonics will be the platform on which these interferometers are constructed.

We have measured the properties of a new concept for interferometer chips, modular chips, produced by the University of Southampton. Of greatest importance are the transmission and the reconfigurability. Light is mainly lost at the chip-fibre interfaces and in the bent waveguides and cross-couplers of the Mach-Zehnder interferometers. Low transmission is the greatest drawback of the Southampton chip architecture and, for the moment being, this hinders quantum experiments with multiple single photons.

We have demonstrated that the current heater-MZI design gives the full range of phase shift that is needed. We also found that we are not capable of fully extinguishing light in one of two MZI output arms. The likely explanation is that we are coupling into additional modes at the cross-couplers. These modes are not bounded by the waveguides, causing light to leak from the system.

The silica-on-silicon integrated photonics chips made in Southampton are a first step to the fabrication of large reconfigurable multiport interferometers. The elegant and compact design of both optical and electronic components can easily be extended to a larger amount of modes. However, the weaknesses mentioned above and the difficulties introduced by the assembly step in the modular architecture need to be addressed before such a many-mode interferometer can be made functional.

*The conclusion drawn from the theoretical results of chapter 3 is given at the end of that chapter and is not discussed here.

Version of March 12, 2017– Created March 12, 2017 - 20:35

Chapter 8

Appendix

8.1 A realistic interferometer with unbalanced distances

Interferometers created in integrated photonics provide sub-wavelength stability, but are not fabricated with this precision. Different paths through the diagram have the same pathlength phase in the idealised picture above, but in reality light may obtain a different phase in each mode. Consider the case of a 4-mode interferometer displayed below:

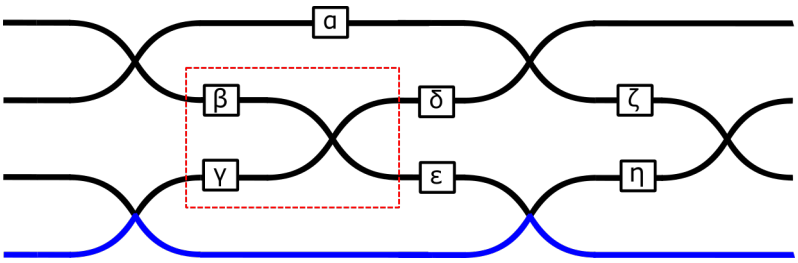

Figure 8.1: *A 4-mode interferometer of the design by Clements et al. [18] with unbalanced distances.*

We take the bottom path (blue) to be our phase reference line. Travelling along the other paths, light acquires a relative phase indicated by the Greek letters. To see how this affects the working of our interferometer, we focus on the beam splitter in the red dotted box, taking phases β and γ into account.

In our interferometers, we use pairs of heaters. Ideally the phases they give are ϕ and $2\pi - \phi$. However, inside the MZI we have introduced

arbitrary path length difference by θ and ι. In front of the MZI we have β and γ. This is depicted in figure 8.2a.

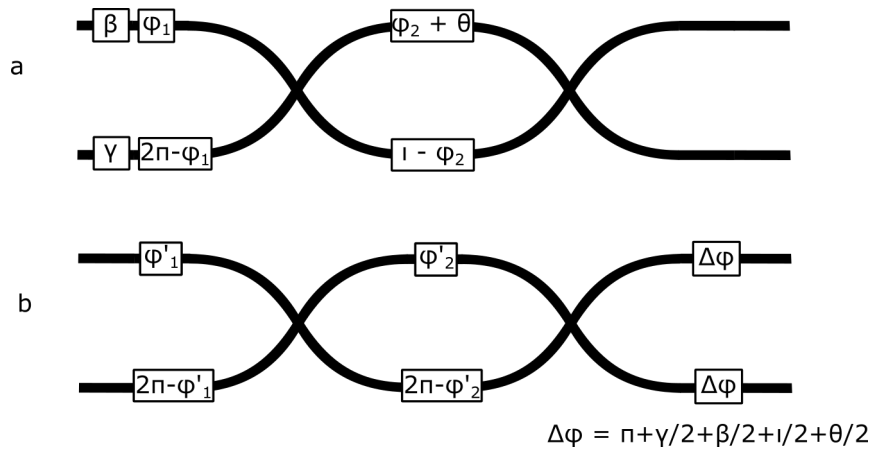

Figure 8.2: *text*

We control phases via the heater setting x that is related linearly to phase, $\phi(x) = ax + b$. The value of b is determined when characterising the network, but we can fully control the phase shift no matter the value of b. We can thus redefine ϕ to include the constants of unbalanced path lengths. If we define $\phi_1' = \phi_1 - \pi - \gamma/2 + \beta/2$ and $\phi_2' = \phi_2 - \iota/2 + \theta/2$, we again have two perfect pairs of phase shifters and one global phase, which can be moved to after the interferometer. This is depicted in figure 8.2b.

When we now return to the large picture, we can now simply redefine δ and ϵ and perform the same procedure on the other beam splitters. In this way, we can actually rewrite the circuit with unbalanced distances as a circuit with perfect distances. The extra phases are captured in the offset of the phase shifters, but during characterisation we can measure this redefined effective phase and determine the offset. We conclude that the unbalanced circuit can function just like the balanced one after we have characterised the phases.

Version of March 12, 2017– Created March 12, 2017 - 20:35

Bibliography

[1] Richard P. Feynman. Simulating physics with computers. *International Journal of Theoretical Physics*, 21(6-7):467–488, 1982.

[2] Paul Benioff. The computer as a physical system: A microscopic quantum mechanical Hamiltonian model of computers as represented by Turing machines. *Journal of Statistical Physics*, 22(5):563–591, 1980.

[3] D Deutsch. Quantum Theory, the Church-Turing Principle and the Universal Quantum Computer. *Proceedings of the Royal Society of London. A. Mathematical and Physical Sciences*, 400(1818):97 LP – 117, jul 1985.

[4] P. Shor. Polynomial-Time Algorithms for Prime Factorization and Discrete Logarithms on a Quantum Computer. *SIAM Journal on Computing*, 26(5):1484–1509, 1997.

[5] Lov K Grover. A Fast Quantum Mechanical Algorithm for Database Search. *Proceedings of the Twenty-eighth Annual ACM Symposium on Theory of Computing*, 1996.

[6] J. I. Cirac and P. Zoller. Quantum computations with cold trapped ions. *Physical Review Letters*, 74(20):4091–4094, 1995.

[7] J E Mooij, T P Orlando, L Levitov, Lin Tian, Caspar H der Wal, and Seth Lloyd. Josephson persistent-current qubit. *Science*, 285(5430):1036–1039, 1999.

[8] Benjamin J Metcalf, Justin B Spring, Peter C Humphreys, Nicholas Thomas-peter, Marco Barbieri, W Steven Kolthammer, Xian-min Jin, Nathan K Langford, Dmytro Kundys, James C Gates, Brian J Smith,

Peter G R Smith, and Ian a Walmsley. Quantum teleportation on a photonic chip. *Nature Photonics*, 8(10):770–774, 2014.

[9] Jacques Carolan, Christopher Harrold, Chris Sparrow, Enrique Martín-López, Nicholas J. Russell, Joshua W. Silverstone, Peter J. Shadbolt, Nobuyuki Matsuda, Manabu Oguma, Mikitaka Itoh, Graham D. Marshall, Mark G. Thompson, Jonathan C. F. Matthews, Toshikazu Hashimoto, Jeremy L. O'Brien, and Anthony Laing. Universal linear optics. *Science*, 349(6249):711–716, 2015.

[10] T Honjo, K Inoue, and H Takahashi. Differential-phase-shift quantum key distribution experiment with a planar light-wave circuit Mach-Zehnder interferometer. *Optics letters*, 29(23):2797–2799, 2004.

[11] C.K. Hong, Z.Y. Ou, and L. Mandel. Measurement of subpicosecond time intervals between two photons by interference. *Phys. Rev. Lett.*, 59, 1987.

[12] Justin B Spring, Benjamin J Metcalf, Peter C Humphreys, W Steven Kolthammer, Xian-Min Jin, Marco Barbieri, Animesh Datta, Nicholas Thomas-Peter, Nathan K Langford, Dmytro Kundys, James C Gates, Brian J Smith, Peter G R Smith, and Ian a Walmsley. Boson sampling on a photonic chip. *Science (New York, N.Y.)*, 339(6121):798–801, 2013.

[13] Andrea Crespi, Roberto Osellame, Roberta Ramponi, Daniel J. Bord, Ernesto F. Galvão, Nicolò Spagnolo, Chiara Vitelli, Enrico Maiorino, Paolo Mataloni, and Fabio Sciarrino. Integrated multimode interferometers with arbitrary designs for photonic boson sampling. *Nature Photonics*, 7, 2013.

[14] Marco Bentivegna, Nicolò Spagnolo, Chiara Vitelli, Fulvio Flamini, Niko Viggianiello, Ludovico Latmiral, Paolo Mataloni, Daniel J. Brod, Ernesto F. Galvão, Andrea Crespi, Roberta Ramponi, Roberto Osellame, and Fabio Sciarrino. Experimental scattershot boson sampling. *Science Advances*, 1(3):e1400255, 2015.

[15] Lieven M K Vandersypen, Matthias Steffen, Gregory Breyta, Costantino S Yannoni, Mark H Sherwood, and Isaac L Chuang. Experimental realization of Shor's quantum factoring algorithm using nuclear magnetic resonance. *Nature*, 414(6866):883–887, 2001.

[16] Scott Aaronson and Alex Arkhipov. The Computational Complexity of Linear Optics. *Theory of Computing*, 9(4):143–252, 2013.

[17] Michael Reck, Anton Zeilinger, Herbert J. Bernstein, and Philip Bertani. Experimental realization of any discrete unitary operator. *Physical Review Letters*, 73(1):58–61, 1994.

[18] William R. Clements, Peter C. Humphreys, Benjamin J. Metcalf, W. Steven Kolthammer, and Ian a. Walmsley. An Optimal Design for Universal Multiport Interferometers. (2):8, 2016.

[19] G. Lepert, M. Trupke, E.a. Hinds, H. Rogers, J.C. Gates, and P.G.R. Smith. Demonstration of UV-written waveguides, Bragg gratings and cavities at 780 nm, and an original experimental measurement of group delay. *Optics Express*, 19(25):24933–24943, 2011.

[20] Dmytro O. Kundys, James C. Gates, Sonali Dasgupta, Corin B E Gawith, and Peter G R Smith. Use of cross-couplers to decrease size of UV written photonic circuits. *IEEE Photonics Technology Letters*, 21(13):947–949, 2009.

[21] H. L. Rogers, S. Ambran, C. Holmes, P. G. R. Smith, and J. C. Gates. In situ loss measurement of direct UV-written waveguides using integrated Bragg gratings. *Optics letters*, 35(17):2849–51, 2010.

[22] William R Clements. Multiphoton Quantum States in Waveguide Networks. *Transfer report, University of Oxford, Lady Margaret Hall*, pages 1–18, 2015.

[23] Jacob Mower, Nicholas C. Harris, Gregory R. Steinbrecher, Yoav Lahini, and Dirk Englund. High-fidelity quantum state evolution in imperfect photonic integrated circuits. *Physical Review A - Atomic, Molecular, and Optical Physics*, 92(3):1–7, 2015.

[24] Andrea Crespi, Roberta Ramponi, Roberto Osellame, Linda Sansoni, Irene Bongioanni, Fabio Sciarrino, Giuseppe Vallone, and Paolo Mataloni. Integrated photonic quantum gates for polarization qubits. *Nature communications*, 2:566, 2011.

[25] Justin B. Spring, Patrick S. Salter, Benjamin J. Metcalf, Peter C. Humphreys, Merritt Moore, Nicholas Thomas-Peter, Marco Barbieri, Xian-Min Jin, Nathan K. Langford, W. Steven Kolthammer, Martin J. Booth, and Ian a. Walmsley. On-chip low loss heralded source of pure single photons. *Optics Express*, 21(11):13522–13532, 2013.

[26] Brice Calkins, Paolo L. Mennea, Adriana E. Lita, Benjamin J. Metcalf, W. Steven Kolthammer, Antia Lamas Linares, Justin B. Spring,

Peter C. Humphreys, Richard P. Mirin, James C. Gates, Peter G. R. Smith, Ian a. Walmsley, Thomas Gerrits, and Sae Woo Nam. High quantum-efficiency photon-number-resolving detector for photonic on-chip information processing. *Optics Express*, 21(19):22657–22670, 2013.